A SIMPLE MODEL SYSTEM FOR IRREGULAR SCATTERING*

C. JUNG

Fachbereich Physik, Universität Bremen
2800 Bremen, Germany

(Received September 30, 1991)

In this lecture the basic ideas of classical scattering chaos are demonstrated with the help of a simple model. The Cantor set of singularities in the deflection function, the invariant set in the phase space and the chaotic structure in the cross section are presented. Within the semiclassical approximation for the quantum cross section it is shown in which way some signs of the classical chaos can show up in the quantum system.

PACS numbers: 05.45.+b, 03.65.Nk, 03.80.+r

1. Introduction

One of the important sources of our knowledge on physical systems is the investigation of scattering events. From measurements of the cross section we can learn something about the interaction between the colliding particles and about their internal structure. The evaluation of cross sections is simple only in those cases, in which the cross section is smooth as function of angle and/or energy. Interestingly, physicists have encountered systems where the cross section is an extremely complicated function showing structure on many scales. For example in nuclear physics such cases are known for about 30 years [1]. Later, complicated behaviour has also been found in classical model computations for molecular reactions (for these processes see the review [2]), for satellite encounters [3], for vortex scattering in hydrodynamics [4], for soliton scattering [5] and for various models of potential scattering (for reviews see [6,7]).

When we find complicated structures on many scales, then we immediately think of fractal structures and chaotic dynamics. When we hear the

* Presented at the IV Symposium on Statistical Physics, Zakopane, Poland, September 19–29, 1991.

expression "chaos in scattering" we may rise the objection, that a typical scattering trajectory cannot be chaotic in the same sense as a bound trajectory is chaotic. A typical scattering trajectory has a simple incoming asymptote and a simple outgoing asymptote and in between the interaction acts for a finite time only. Accordingly, a scattering trajectory can show complicated behaviour for a finite time at most. However, usually we call a trajectory chaotic only if it shows complicated behaviour for ever and therefore a typical scattering trajectory can never be chaotic. We see; If chaos in scattering systems exists at all, then it works in a more subtile way. It is the purpose of this lecture to show in which way genuine chaos can occur in scattering systems and how it shows up in measurable quantities, in particular in the cross section.

To do this we study a particular model system which is well suited for pedagogical purposes and we indicate, to which extend the properties of this particular model represent the general situation of scattering chaos. For simplicity we take a system with 2 degrees of freedom where a point particle moves in a 2-dimensional position space under the influence of a local potential V. We choose the following system which has been investigated thoroughly [8-13];

$$V(x,y) = \exp[-y^2 - (x+\sqrt{2})^2] + \exp[-(y-\sqrt{3/2})^2 - (x-\sqrt{1/2})^2] + \exp[-(y+\sqrt{3/2})^2 - (x-\sqrt{1/2})^2] \quad (1)$$

x, y are Cartesian coordinates in the position space. We use the notation p_x, p_y for the canonically conjugate momenta and $r = \sqrt{x^2+y^2}$. Our considerations are valid for potentials which decrease sufficiently fast for $r \to \infty$ such that all asymptotic conditions of scattering theory are fulfilled, in particular we need that

$$\lim_{r\to\infty} rV(x,y) = 0\,. \quad (2)$$

Thereby we exclude interactions of the Coulomb type which violate this condition. The treatment of irregular Coulomb scattering will be explained in the lecture by L. Wiesenfeld.

System (1) is invariant under rotations by $\pm 2\pi/3$. The potential has 7 critical points; one relative minimum $P_0 = (0,0)$ at energy $E_0 = 0.40\cdots$, three saddle points P_{S1}, P_{S2}, P_{S3} at energy $E_S = 0.459\cdots$, and three maxima P_{M1}, P_{M2}, P_{M3} at energy $E_M = 1.005\cdots$. $P_{S1} = (0.6\cdots, 0)$ and the coordinates of P_{S2} and P_{S3} are obtained by rotating P_{S1} around $\pm 2\pi/3$. $P_{M1} = (-1.4\cdots, 0)$ and the coordinates of P_{M2} and P_{M3} are obtained by rotating P_{M1} around $\pm 2\pi/3$.

2. Cantor set of singularities in the deflection function

First we look for signs of chaos in the scattering dynamics of system (1) in the form of a fractal structure in the deflection function. Incoming asymptotes are labelled by the following three quantities; The initial asymptotic energy $E_{\text{in}} = \vec{p}_{\text{in}}^{\,2}$, the incoming direction $\alpha = \arctan(p_{x,\text{in}}/p_{y,\text{in}})$ and the impact parameter $b = (x\,p_{y,\text{in}} - y\,p_{x,\text{in}})/\sqrt{2\,E}$. The scattering angle θ of a given trajectory is the difference between the outgoing direction and the incoming direction taken modulo 2π. The deflection function is the scattering angle θ as function of b for fixed E and α.

Fig. 1(a) shows the deflection function for model system (1) in the interval $b \in [-3, +3]$. For b outside of this interval the incoming projectile misses the region where the potential is essentially different from zero and there is hardly any deflection. In Fig. 1(a) we see four places where θ changes very rapidly in a complicated way as b varies. Fig. 1(b) gives a magnification of the vicinity of such a place. One of the structures of Fig. 1(a) is resolved into several complicated looking substructures. In Fig. 1(c) such a substructure is magnified further and a set of even smaller substructures becomes visible. Fig. 1(c) looks very similar to Fig. 1(b). Such a magnification can be repeated any number of times and we always obtain similar plots. This self-similarity of the structure under magnification is typical for Cantor sets.

In these figures we have labelled the gaps of the Cantor set by finite sequences of the letters R (standing for right) and L (standing for left). The rules for this signature are as follows; on the magnification level 1 (see Fig. 1(a)) we assign the symbol L to the gap between -0.49 and -0.35 and the symbol R to the gap between 0.35 and 0.49. Under magnification new gaps, *i.e.* intervals of continuity of the deflection function, appear near the ends of the intervals L and R. These gaps of level 2 are denoted by sequences of two letters. The first letter is the same as the letter of the nearby gap of level 1. The second letter becomes L or R according to whether the gap of level 2 lies to the left or right of the nearby gap of level 1. We continue this scheme by induction. In system (1) we find 2^{n+1} gaps of level $n+1$ and they appear near the ends of the gaps of level n. The signature for gaps of level $n+1$ consists of $n+1$ letters. The first n letters are the signature of the neighbouring gap of level n. The last letter is L or R according to whether the new gap lies to the left or to the right of the corresponding interval of level n. The points of the Cantor set itself, which is the set of accumulation points of boundary points of gaps, are labelled by infinite L/R sequences such that the symbol sequence of such a point is the limit of the symbol sequences of gaps, which converge to this point.

A first indication on the origin of the observed fractal structure in the deflection function can be obtained by looking at some trajectories in po-

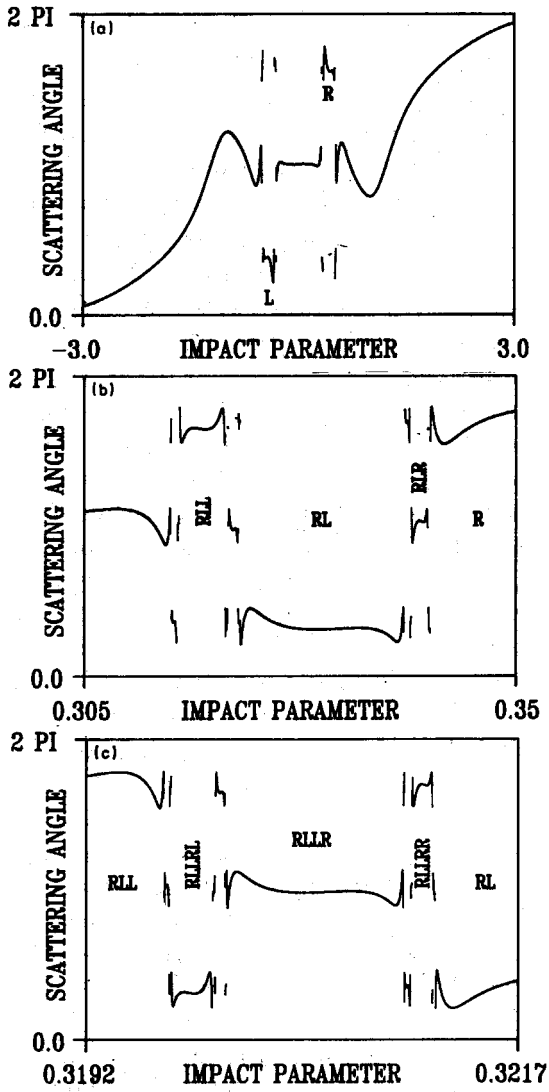

Fig. 1. Scattering angle as a function of the impact parameter for energy $E = 0.6$ and incoming direction $\alpha = \pi$. Part (a) gives an overview of the interval $b \in [-3, +3]$. Part (b) displayes a magnification of an interesting region of b values and part (c) gives a further magnification.

sition space. Six examples are shown in Fig. 2. In part (a) the scattering trajectory comes in and moves along a closed ring trajectory (called Γ in the following) several times and goes off to infinity again. In part (b) the trajectory comes in and starts oscillating between two potential mountains. Finally it separates from the oscillating trajectory and moves out again.

There are similar oscillating trajectories between the other two pairs of potential mountains. In the following γ_i denotes the oscillating trajectory which passes near the saddle point P_{Si}. In Fig. 2(c) the scattering trajectory first moves along γ_1, then switches to Γ and after a few turns along Γ goes off again. Part (d) shows a scattering trajectory which switches periodically between γ_1 and Γ several times before it leaves the potential region again. In Fig. 2(e) the middle part of the trajectory is a sequence of pieces resembling $^1/_3\Gamma$ and successive γ_i in alternation. Part (f) shows an irregular switching between pieces of the various periodic orbits.

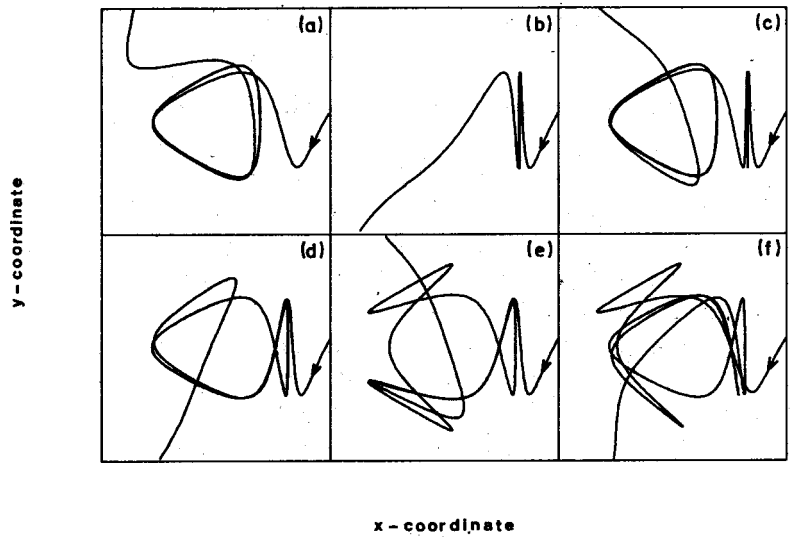

Fig. 2. Six scattering trajectories in position space. The horizontal axis gives x, the vertical axis gives y. All trajectories have energy $E = 0.6$ and incoming direction $\alpha = \pi$. The impact parameters and the labels of their intervals are; (a); $b = 0.5019226 \in$ RRRLRLRLRLR; (b); $b = 0.5151908 \in$ RRRRRR; (c); $b = 0.51519004499 \in$ RRRRRRLRLRLRLR; (d); $b = 0.513933870501 \in$ RRRLRLLLRLRRRLR; (e); $b = 0.513564345433 \in$ RRRLLLRRRLLLRR; (f); $b = 0.49741285802 \in$ RRLLLRRLRRLRLLL.

To obtain such trajectories, it is necessary to carefully choose b from the very small intervals that carry the appropriate L/R signatures given in the figure captions. The relation between signature of the intervals and the qualitative structure of the scattering trajectory is as follows; By S_n we denote the symbol in position number n in the sequence. RR in position 1 and 2 give an incoming part of the scattering trajectory of the kind shown in Fig. 2. If the symbol S_{n+1} is equal to S_n then we add an arc to the trajectory, which is qualitatively similar to $^1/_2\gamma_i$. Out of the various six posibilities for $^1/_2$, γ_i we choose the one which continues the trajectory

smoothly. Likewise, if $S_{n+1} \neq S_n$, then we add an arc qualitatively similar to $^1/_3\Gamma$ with the appropriate orientation to continue the trajectory smoothly. When all symbols of the finite sequence are used up, we add an outgoing part, leaving the interior of the interaction region through the pass opposite to the sector into which the trajectory has to be continued smoothly. This rules can be checked immediately for all six trajectories of Fig. 2. If any type of trajectory is searched for, we decompose it into $^1/_2\gamma$ parts and $^1/_3\Gamma$ parts, construct the corresponding L/R signature and know in which b–interval the trajectory has to start. For trajectories belonging to b–intervals, whose symbol sequence does not start with RR, similar rules can be given with some modifications for symbols in the first three positions.

3. Invariant set and periodic orbits

Because of their importance for the following considerations let us give some more information on the periodic orbits γ and Γ. The orbit Γ exists for energies between E_0 and E_M. At E_0 it emerges from the point P_0. By λ and $1/\lambda$ we denote the eigenvalues of the fixed point belonging to Γ in a Poincare section. At E_0 we find $\lambda = 1$ because of the following reason; the potential V has C_{3v} symmetry. Therefore the expansion of the potential around the origin up to second order must be isotropic, *i.e.* V has an expansion $V(x,y) = E_0 + a(x^2 + y^2)/2$ plus higher-order terms, where $a = 6\exp(-2)$. As long as the energy is infinitesimally above E_0 the particle starting near the origin moves in a two-dimensional isotropic oscillator potential. The frequencies of the two normal modes are degenerate and all trajectories are periodic and have the same recurrence time $T = 2\pi/\sqrt{a}$. Accordingly, for $E \to E_0$ from above, all points near the origin become fixed points in the Poincare section. Both eigenvalues are one for all these points. For increasing E the higher-order terms in the potential become important, the isotropy of the potential is destroyed and from the two-dimensional continuum of fixed points in the Poincare section only the fixed point belonging to the periodic orbit Γ survives.

With increasing energy, Γ remains at first elliptic. λ wanders around the upper half of the unit circle until at an energy slightly below E_S it meets the value -1. Here Γ switches from elliptic to inverse hyperbolic. With further increase of the energy λ wanders along the negative real axis. At $E = 0.6$, which will be used mainly in the following, its value is $\lambda \approx -83$. For $E \to E_M$ we find $\lambda \to -\infty$.

The orbits γ_i exist for energies between E_S and E_M; their eigenvalues will be denoted by $\mu, 1/\mu$. Again, these eigenvalues refer to the eigenvalues of the corresponding fixed point in a Poincare section. At $E = E_S$ the orbits γ_i emerge from the points P_{Si} with eigenvalues $\mu \approx 47$. With increasing

energy μ increases too. At $E = 0.6$ we find $\mu \approx 107$ and for $E \to E_M$ we find $\mu \to +\infty$. The value of μ at E_S can be checked analytically; Around P_{S1} the potential can be approximated quadratically as $V(x,y) = E_S - a(x - x_S)^2/2 + by^2/2$ plus higher-order terms, where $a \approx 0.660\cdots$ and $b \approx 1.747\cdots$. Accordingly, for energies slightly above E_S the orbit γ_1 has the form

$$x(t) = x_{S1}; \quad y(t) = y_0 \cos(\sqrt{b}t + \varphi_0)\,. \tag{3}$$

The recurrence time of this orbit is $T = 2\pi/\sqrt{b}$. Small deviations in the x direction develop like

$$x(t) - x_{S1} = x_+ \exp(\sqrt{a}t) + x_- \exp(-\sqrt{a}t)\,. \tag{4}$$

During the time T the unstable solution is amplified by the factor $\mu = \exp(2\pi\sqrt{a/b}) \approx 47.\cdots$.

Fig. 2 strongly indicates that the periodic orbits γ and Γ and their heteroclinic and homoclinic connections play an important role in the creation of the complicated scattering behaviour found in the deflection function. Those trajectories of the system, which are held between the three potential mountains for all times in past and future will be called localised in the following. The properties of these orbits can be investigated best in an appropriate Poincare section. For system (1) we can construct a Poincare section which is adapted to the C_{3v}–symmetry of the potential as follows;

Fig. 3 shows the equipotential lines of the potential for $E = 0.6$ together with three symmetry lines $\sigma_1, \sigma_2, \sigma_3$ and two pieces of orbits. It turns out to be useful to define the σ_i as half lines rather than full lines. So they start at P_0 and extend straight to infinity. V is invariant under reflections at σ_i. The set of the three σ_i lines is itself invariant under C_{3v} operations.

For energies not too close to E_S, namely for $E > E_B \approx 0.485\cdots$ localised orbits do not enter a neighbourhood of the origin. Therefore, for any localised orbit, and thus in particular for any periodic orbit, the sequence of crossings of the σ_i lines can be followed. Divide the trajectory into pieces as given by subsequent σ_i crossings. Let $d_j = k$ if the jth crossing occurs at the line σ_k. For each trajectory, this allows the construction of a 0/1 sequence according to the scheme

$$a_j = 0 \quad \text{if} \quad d_{j+1} = d_j\,,$$
$$a_j = 1 \quad \text{if} \quad d_{j+1} \neq d_j\,.$$

It is intuitively clear that a binary sequence is adequate as can be seen from Fig. 3. Let an orbit cross line σ_1 with positive $\dot{y}$. The next crossing is either with line σ_1 again or with line σ_2 as shown in the two pieces of orbit shown in Fig. 3. Thus after each crossing there is a binary choice; to return to the line of the last crossing or to go on to the next line.

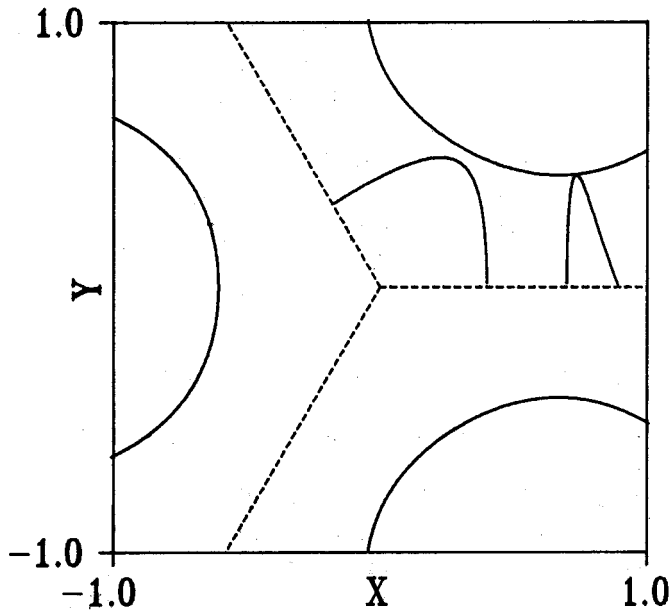

Fig. 3. The energy boundary for $E = 0.6$ (three full line segments starting and ending at the frame boundary), the symmetry lines $\sigma_1, \sigma_2, \sigma_3$ (three broken half lines emanating from the origin), and two pieces of orbits in position space. The right piece is of $1/2\gamma$ type; it returns to the σ line from which it started. The other piece is of $1/3\Gamma$ type; it connects two different σ lines.

Two periodic orbits are particularly simple. First, the orbit γ, which oscillates back and forth across one of the three saddles. It corresponds to $a_j = 0$ for all j. There are of course three such orbits, but as they are related by C_{3v} symmetry we shall identify them as one orbit γ. Second, the ring orbit Γ corresponding to $a_j = 1$ for all j. This orbit rotates around the origin in one of the two possible orientations. Because these two orientations are related by reflections at σ_i they will be identified as one orbit Γ.

Other localized orbits can be described as follows; Each $a_j = 0$ in the sequence corresponds to a piece of orbit which resembles $^1/_2\gamma$ and each $a_j = 1$ corresponds to a piece which resembles $^1/_3\Gamma$. This is the same type of decomposition which has been done for the middle parts of scattering trajectories in the last section. Periodic orbits correspond to periodic symbolic sequences where some basic block of symbols is repeated for ever. Fig. 4 shows some examples of periodic orbits at energy $E = 0.6$. The basic block of the signature is indicated for each orbit in the figure. In part (q) only one half and in parts (p) and (r) only one third of the complete orbit is displayed. To get the complete orbit, the displayed pieces of the orbit have to be supplemented symmetrically, what can be done easily with the help

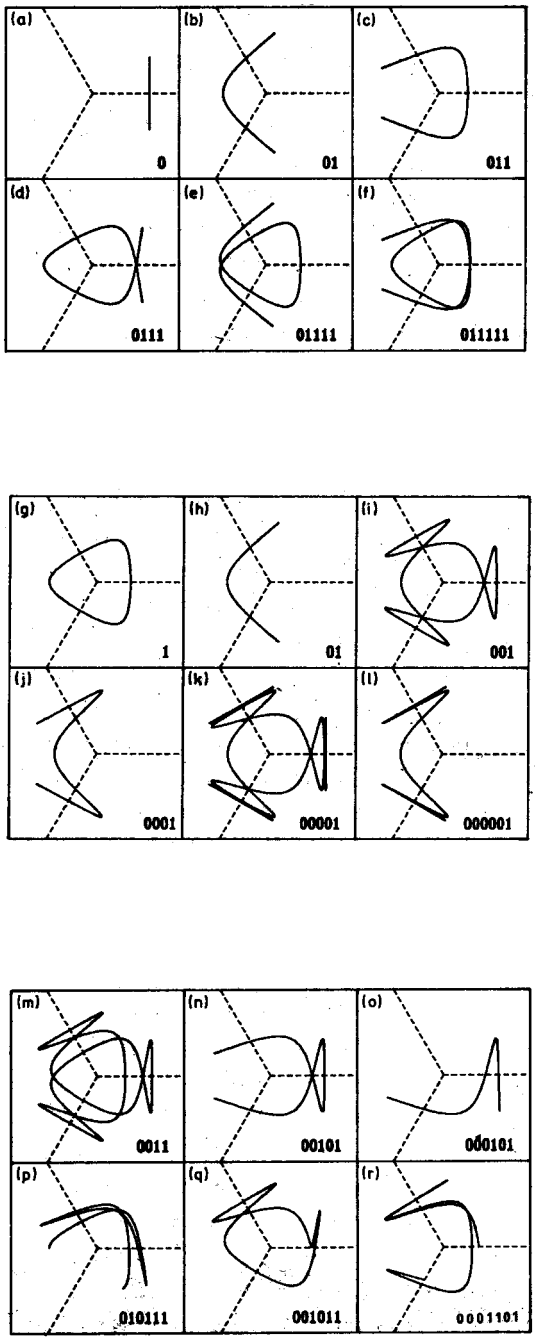

Fig. 4. 18 examples of periodic orbits of low periods in position space. To each orbit we give the basic block of the periodic symbolic sequence in the lower right corner.

of the symmetry lines shown.

The construction of the Poincare mapping itself is done in the following way: Let the energy be fixed at a value E. For each crossing of a trajectory with any of the lines σ_1 , σ_2 or σ_3 we record the distance r from the origin and the radial component p_r of the momentum, *i.e.* its projection on σ_i. Both orientations of crossings are taken because σ_i are half lines. The surface of section $\mathcal{P}$ so defined is invariant under C_{3v} operations. A given point $z \in \mathcal{P}$ thus represents six different phase space points which will be identified.

Each localized orbit generates an infinite sequence of intersections with the r/p_r plane. Generic scattering trajectories, on the other hand, produce finite sets of points. In the energy interval $E \in (E_S, E_M)$ almost all initial points in $\mathcal{P}$ correspond to scattering orbits with incoming and outgoing asymptotes. They have a first and a last intersection with the lines σ_i. The set Λ_+ of points in $\mathcal{P}$ which possess infinitely many images under the Poincare map $P : \mathcal{P} \to \mathcal{P}$ has measure zero. Likewise, the set Λ_- of points with infinitely many preimages has also measure zero. The localised orbits correspond to the set $\Lambda = \Lambda_+ \cap \Lambda_-$. In particular, Λ contains all periodic points of the map P and they represent the periodic orbits of the system.

Λ can be constructed from the structure of the stable manifold W^s and the unstable manifold W^u of the fixed point P_γ of the Poincare map, which corresponds to the periodic orbit γ. Some branches of these manifolds are shown in Fig. 5 for $E = 0.6$. The branch X of W^u extends directly into the asymptotic range $r \to \infty$. The inner branch A of W^u leaves P_γ towards the point a_- at $r = 0$ from where it jumps to the point a_+ because the intersection of the corresponding orbit is now with a different σ_i line, and the projection of the momentum is therefore different. The next piece B continues towards larger r values and passes near P_γ before it returns to $r = 0$ at the point b_-. From there W^u leaves the frame of Fig. 5 and reenters later at the point c_+. The last two pieces shown are C and D. Of course, there is an infinity of further branches of W^u which are not shown in the figure. They all lie between $A \cup X$ and B. Because of symmetry W^s is the mirror image of W^u created by reflection in the line $p_r = 0$. The corresponding branches of W^s are labelled by overbared letters.

The homoclinic intersections between W^u and W^s are confined to the shaded area in Fig. 5. It also contains the set Λ, which is the topological closure of these homoclinic intersections. The action of the Poincare map in the shaded area is a perfect example of Smale's horseshoe construction as long as the energy is restricted to the interval (E_B, E_M). Next let us understand this construction in more detail.

Fig. 6 gives a schematic plot of this shaded area. The nature of the map becomes clear if we consider some special points on the invariant manifolds.

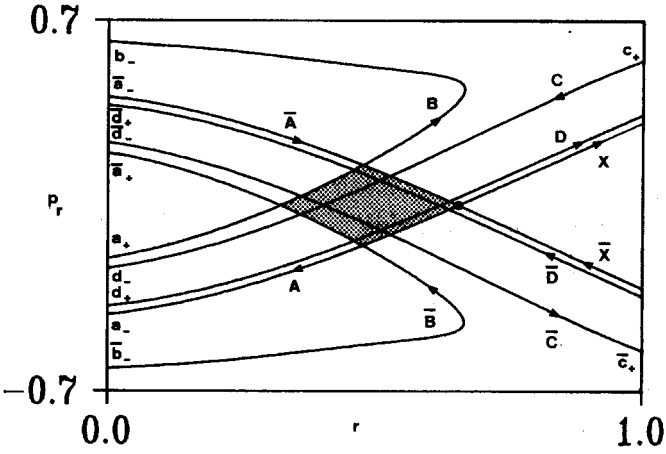

Fig. 5. Some branches of the invariant manifolds of the fixed point P_γ (marked by a full circle) in the r/p_r plane, for $E = 0.6$. All localised orbits of the Poincare map P are located within the hatched area.

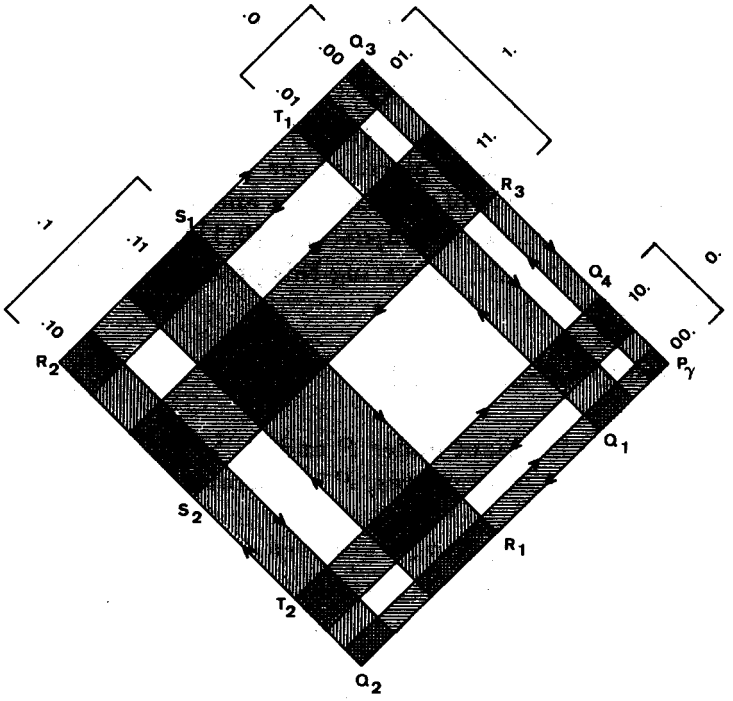

Fig. 6. Schematic plot of the horseshoe dynamics in the hatched area of Fig. 5.

Under the mapping P we find

$Q_1 \mapsto Q_2 \mapsto Q_3 \mapsto Q_4$
$R_1 \mapsto R_2 \mapsto R_3$
$S_1 \mapsto S_2$
$T_1 \mapsto T_2$
If we define the four rectangles
$.0 := P_\gamma Q_1 T_1 Q_3$
$0. := P_\gamma Q_2 T_2 Q_4$
$.1 := R_1 Q_2 R_2 S_1$
$1. := R_2 Q_3 R_3 S_2$
we have the mapping
$P : .0 \cup .1 \mapsto 0. \cup 1.$
$.0 \mapsto 0.$
$.1 \mapsto 1.$

In order to construct the sets $\Lambda_+, \Lambda_-, \Lambda$ recursively, we introduce the notation
$\Lambda_+^1; = \{.0, .1\}, \Lambda_-^1; = \{0., 1.\}$
for the two sets of rectangles, and
$\Lambda^1; = \{a_{-1}.a_1 = a_{-1}. \cap .a_1 | a_j \in \{0,1\}\}$
for the set of their four intersections $0.0, 0.1, 1.0, 1.1$, with $\Lambda^1 = \Lambda_+^1 \cap \Lambda_-^1$. On Λ^1 both P and its inverse are defined. Thus we can define the images and preimages of the four parts;
$\Lambda_+^2; = \{.a_1 a_2 = P^{-1}(a_1.a_2) | a_j \in \{0,1\}\}$
$\Lambda_-^2; = \{a_{-2}a_{-1}. = P(a_{-2}.a_{-1}) | a_j \in \{0,1\}\}.$
All these strips are bounded by pieces of the invariant manifolds. The set of their intersections consists of sixteen parts and will be called Λ^2;
$\Lambda^2; = \{a_{-2}a_{-1}.a_1 a_2 = a_{-2}a_{-1}. \cap .a_1 a_2 | a_j \in \{0,1\}\}.$
Again we have $\Lambda^2 = \Lambda_+^2 \cap \Lambda_-^2$. Iterating this procedure we obtain a nested sequence of sets $\Lambda^n = \Lambda_+^n \cap \Lambda_-^n$
$\Lambda^1 \supset \Lambda^2 \supset \cdots \supset \Lambda^n \supset$
each consisting of 2^{2n} elements with
$\Lambda = \bigcap_{n=1}^{\infty} \Lambda^n$.
By construction, Λ is invariant under P and P^{-1}. The operation of P is a right shift on the symbolic sequences, P^{-1} operates as a left shift;

$$P : \cdots a_{-n} \cdots a_{-2}a_{-1}.a_1 a_2 \cdots a_n \cdots \mapsto \cdots a_{-n} \cdots a_{-2}a_{-1}a_1.a_2 \cdots a_n \cdots$$
$$P^{-1} : \cdots a_{-n} \cdots a_{-2}a_{-1}.a_1 a_2 \cdots a_n \cdots \mapsto \cdots a_{-n} \cdots a_{-2}.a_{-1}a_1 a_2 \cdots a_n \cdots$$

In the phase space there corresponds to the set Λ a chaotic saddle consisting of an countable infinity of unstable periodic orbits and an overcountable infinity of unstable nonperiodic localised orbits. They all have their

own stable manifolds going out into the asymptotic region. Therefore, in the asymptotic region there is an bundle of stable manifolds of localised orbits. Transversal to the sheets of the bundle we find a Cantor set structure. The genuine scattering trajectories flow through the gaps of the chaotic saddle and cast some kind of shadow image of it into the outgoing asymptotic region. Whenever the initial condition of a scattering trajectory lies on one of these stable manifolds, the trajectory will get stuck in the potential interior and the scattering angle is undefined. Thereby each localised orbit in the chaotic saddle has an influence on the scattering behaviour similar to the influence of a circular periodic orbit in the orbiting effect in rotationally symmetric systems.

The set of singularities of the deflection function in the set of all possible initial asymptotes is a subset of measure zero. Therefore we do not hit the singularities exactly in numerical computations or in an actual experiment. What we see is a jump of the scattering angle whenever the initial condition jumps from one side of a stable manifold of a localised orbit to the other side. Scattering trajectories belonging to adjacent gaps of the Cantor set, having one letter more or one letter less in their signature, leave the potential interior through different saddles and therefore their scattering angles differ by approximately $\pm 2\pi/3$. Actually between these two intervals there is an infinite number of additional smaller intervals with longer signatures. Therefore by scanning b in finer and finer steps through tiny regions the scattering angle is seen to make more and more jumps of approximately $\pm 2\pi/3$ each time. This is exactly what we have seen in Fig. 1.

All essential properties of the chaotic saddle can be reconstructed from measurements of the deflection function. The quantitative evaluation of the chaotic saddle will be explained in detail in the lecture by T. Tel. For more information on transient chaos and its application to scattering see [14-16].

4. Rainbows in the classical cross section

Unfortunately, the deflection function is hard to obtain even in experiments on macroscopic systems and it is not at all measurable in microsystems. Its measurement would require an exact preparation of momentum and impact parameter of the projectile. In usual scattering experiments the momentum is specified as precisely as possible and the impact parameter is completely unspecified. The quantity which is really measured is the differential cross section as a function of angle and/or energy. The maximal information which can be obtained from a scattering experiment on microsystems is provided by the differential cross section. In this section we shall explain in which way the chaos in the phase space and the existence of a chaotic saddle show up in the cross section.

The computation of the cross section is done like this; We fix the energy E and the incoming direction α and take the scattering angle θ as function of the impact parameter b. We determine all values b_j of the impact parameter which lead to some particular scattering angle θ_0, *i.e.* we look for all solutions of $\theta(b) = \theta_0$. For each solution the quantity $(d\theta/db)(b_j)$ is formed and the value of the cross section for the angle value θ_0 is summed up as

$$\frac{d\sigma}{d\theta}(\theta_0) = \sum_j \left(\left| \frac{d\theta}{db}(b_j) \right| \right)^{-1} . \tag{5}$$

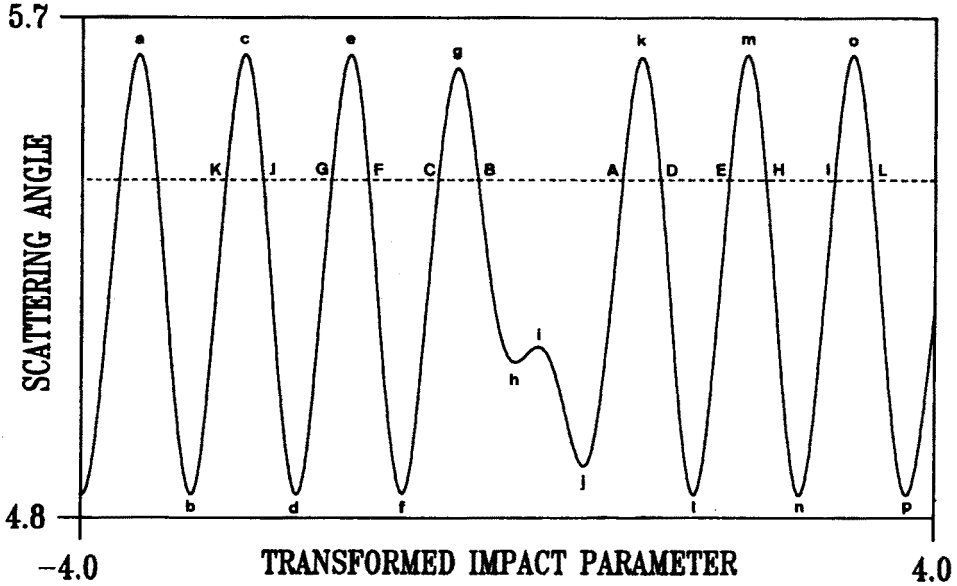

Fig. 7. The deflection function $\theta(B)$ for interval R in logarithmically transformed coordinates according to Eq.(6). The contributions for $\theta = 5.4$ are labelled by capital letters. The extremal values are labelled by lower case letters.

Because of this additivity we first look at the contributions coming from one interval of continuity of the deflection function and delay the summation over all intervals for the moment. As an example we choose the interval R and take $E = 0.6, \alpha = \pi$. This interval corresponds to $b \in (b_{R-}, b_{R+}) = (0.34106\cdots, 0.49733\cdots)$. This interval gives the most important contribution for angle values close to $\theta = 5\pi/3$. In Fig. 1 the behaviour close to the boundaries of the interval R is not well resolved. Therefore Fig. 7 shows the deflection function in the interval R again, this time as a function of the logarithmically transformed impact parameter

$$B = \frac{\ln[(b - b_{R-})/(b_{R+} - b)]}{\ln \mu}, \tag{6}$$

where μ is the eigenvalue of the periodic orbit γ . At energy $E = 0.6$ its value is close to 107. By transformation (6) the interval (b_{R-}, b_{R+}) is mapped one-to-one onto $(-\infty, +\infty)$. For $B \to +\infty$ the deflection function as a function of B can be fitted quite well by the closed form expression

$$\theta(B) \to \frac{5\pi}{3} + \theta_M[1 - c_{R+} \exp(-B \ln \mu)] \sin(2\pi B + \phi_{R+}) \tag{7}$$

and in the same way for $B \to -\infty$ by

$$\theta(B) \to \frac{5\pi}{3} + \theta_M[1 - c_{R-} \exp(B \ln \mu)] \sin(2\pi B + \phi_{R-}), \tag{8}$$

where $\theta_M = 0.394875\cdots$.

The approximate periodicity of $\theta(B)$ for $B \to \pm\infty$ can be understood as follows; If b is close to the boundary of the interval of continuity, then the trajectory in position space performs oscillations on the saddle before it leaves the potential region. If the value of b comes closer to b_{R+} or b_{R-} by a factor μ, then the trajectory in position space spends one more period along γ. Accordingly, the factor $1/\ln \mu$ in (6), together with the sin function in (7) ensures that $\theta(B)$ assumes the same value. For b values in between, all angle values are obtained which can be reached by trajectories leaving the periodic orbit γ close to its unstable manifold.

To understand the slight deviation from periodicity note that, when the scattering trajectory moves along γ for some additional turns, more energy is put into the transverse motion, and the deviation of the angle value from its middle value $5\pi/3$ can become greater. In the extreme case of $b \to b_{R\pm}$ the amplitude of the oscillations of the scattering angle converges to θ_M. This approach of the oscillations to their maximal amplitude is adequately described by the factor $[1 - c_{R\pm} \exp(\mp \ln \mu)]$ in (7) and (8). The behaviour of $\theta(B)$ close to $B = 0$ is determined by the particular value of the energy, and there is no simple analytical fit for it.

Fig. 8 shows the contribution of the interval R to the cross section. Each relative extremum of $\theta(b)$, where $d\theta/db = 0$, gives a singularity in the cross section, a so called rainbow. We have marked the extrema in Fig. 7 and the corresponding singularities in Fig. 8 by matching letters. In Fig. 8 we have chosen logarithmic scales on both axes in order to demonstrate the simple scaling properties of the system. The abscissa gives the transformed scattering angle;

$$\psi(\theta) = \frac{\ln[(\theta - 5\pi/3 + \theta_M)(5\pi/3 + \theta_M - \theta)^{-1}]}{\ln \mu}. \tag{9}$$

In these coordinates the angular distance between any rainbow and its successor (the one coming from the neighbouring extremum in Fig. 7) becomes

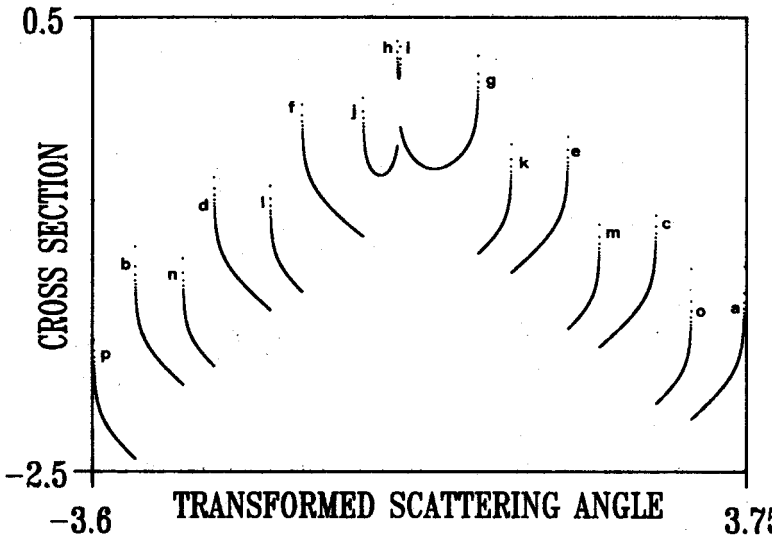

Fig. 8. Contribution of the interval R to the differential cross section. The logarithm of the cross section is plotted as a function of the logarithmically transformed scattering angle (9). The rainbow singularities of the cross section are labelled to indicate the one-to-one correspondence between the rainbows and the extrema of the deflection function shown in Fig. 7.

1 in the limit $B \to \infty$. Compare e.g. the distance between p and n, or b and d, or m and o, *etc.* Along the ordinate the quantity $\ln(d\sigma/d\theta)/\ln\mu$ is plotted. We notice that each branch is shifted vertically by approximately $^1/_2$, as compared to its successor. The reason is as follows; Close to a maximum of $\theta(b)$ at $b = b_n$ with angle value $\theta = \theta_n$ we approximate $\theta(b) = \theta_n - A(b - b_n)^2/2$ and find

$$\left|\frac{d\theta}{db}(b_n)\right| = |A(b - b_n)| = [2(\theta_n - \theta)A]^{1/2}. \tag{10}$$

Close to the neighbouring maximum at b_{n+1} with angle value θ_{n+1} we approximate $\theta(b) = \theta_{n+1} - A\mu^2(b - b_{n+1})^2/2$ and find

$$\left|\frac{d\theta}{db}(b_{n+1})\right| = |A\mu^2(b - b_{n+1})| = \mu[2(\theta_{n+1} - \theta)A]^{1/2}, \tag{11}$$

where, according to (6) and (7), the b_n and θ_n scale as $b_{R+} - b_n \approx \mu(b_{R+} - b_{n+1})$ and $5\pi/3 + \theta_M - \theta_n \approx \mu(5\pi/3 + \theta_M - \theta_{n+1})$. Let $\psi_n = \psi(\theta_n)$ and $\psi_{n+1} = \psi(\theta_{n+1})$ be the transformed scattering angles at θ_n, θ_{n+1}. We compare the cross section at two angle values $\bar{\psi}$ and $\tilde{\psi}$ which lie close to ψ_n and ψ_{n+1} respectively such that

$$\psi_n - \bar{\psi} = \psi_{n+1} - \tilde{\psi} \ll 1, \tag{12}$$

where $\bar{\psi}$ and $\tilde{\psi}$ correspond to the values $\bar{\theta}$ and $\tilde{\theta}$ of the original angle θ. Eqs (6) and (7) imply $\theta_n - \bar{\theta} \approx \mu(\theta_{n+1} - \tilde{\theta})$. Inserting this into (10) and (11) leads to

$$\left|\frac{d\theta}{db}(\tilde{\theta})\right| = \mu[2A(\theta_{n+1} - \tilde{\theta})]^{1/2} = [2A\mu(\theta_n - \bar{\theta})]^{1/2} = \mu^{1/2}\left|\frac{d\theta}{db}(\bar{\theta})\right|. \quad (13)$$

Accordingly, for the ratio between the contributions to the cross section coming from the vicinities of the two maxima we obtain

$$\frac{d\sigma}{d\theta}(\tilde{\theta}) = \mu^{-1/2}\frac{d\sigma}{d\theta}(\bar{\theta}) \quad (14)$$

or

$$\frac{\ln \frac{d\sigma}{d\theta}(\tilde{\theta})}{\ln \mu} = \frac{\ln \frac{d\sigma}{d\theta}(\bar{\theta})}{\ln \mu - \frac{1}{2}}. \quad (15)$$

Analogous considerations hold for the minima.

At the energy $E = 0.6$ the two extrema of $\theta(b)$ in the middle of the interval, labelled by h and i in Fig. 7, are not separated very much in their θ values. This causes a corresponding double singularity in the cross section which comes close to a cubic rainbow. It forms the most prominent structure in the cross section.

The next step is, to demonstrate that all intervals of continuity give similar contributions to the cross section. This can be done as follows; We take an interval of continuity of the impact parameter line (at fixed incoming angle) and transport it by the flow through the potential until it reaches the region of outgoing asymptotes. There we make a plot of the values of the scattering angle and the outgoing angular momentum L, which is equivalent to the outgoing impact parameter. Thereby an interval of continuity of the incoming impact parameter line is mapped onto a continuous curve in the θ/L plane. Fig. 9 shows the results for the three intervals R, LL, LR. All other intervals that lead to θ values around $5\pi/3$, give spiral lines which run alongside these three lines in qualitatively the same manner. The only difference between these various spirals is a shift of the middle structure which produces the almost cubic rainbow structure in the cross section. The outer boundary line of the spirals is the intersection between the asymptotic θ/L plane and that branch of the unstable manifold W^u of γ which leaves the potential directly outwards (branch X in Fig. 5). The image of any b interval spirals towards this boundary line in such a way that for each complete turn the distance from the boundary decreases by a factor μ. If a position space trajectory makes one more turn along γ, then it lies closer to the unstable manifold W^u by a factor μ. Spirals from different intervals are not allowed to intersect each other. Therefore, all spirals must converge

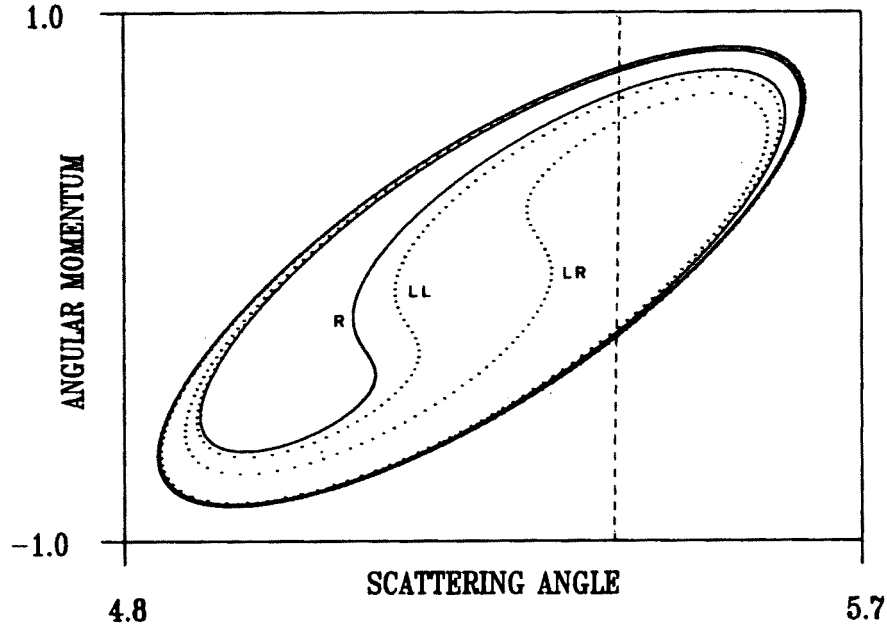

Fig. 9. Intersection between the outgoing asymptotic plane and the trajectories starting in the intervals R, LL, LR with $E = 0.6$ and $\alpha = \pi$. The scattering angle value $\theta = 5.4$ is marked by a broken line.

to the boundary line by the same rate. This universal scaling behaviour for all intervals originates from the fact that the boundary points of the various intervals all lie on the stable manifold of the same periodic saddle trajectory γ.

In this sense the scaling behaviour of all intervals is the same as the one described in detail for interval R, and the structure of the analytical fit of (7) and (8) holds for any interval. For the various intervals we have only to insert other boundary values b_+, b_- for the impact parameter transformation in Eq. (6) and other constants c_+, c_-, ϕ_+, ϕ_- in (7) and (8).

There is a natural one-to-one correspondence between the extremal angle values of the deflection function in interval R and the extremal values of the deflection function in other intervals. Therefore, all intervals create qualitatively the same rainbow structures in their contributions to the cross section. There are only two differences between the various contributions. First, the exact values of the rainbow angles are slightly shifted according to the shift of the spirals in Fig. 9. Second, the total weight of the contribution of any interval is proportional to its length *i.e.* proportional to the amount of incoming flux which falls into this interval.

Fig. 10 presents the cross section of the combined contributions from

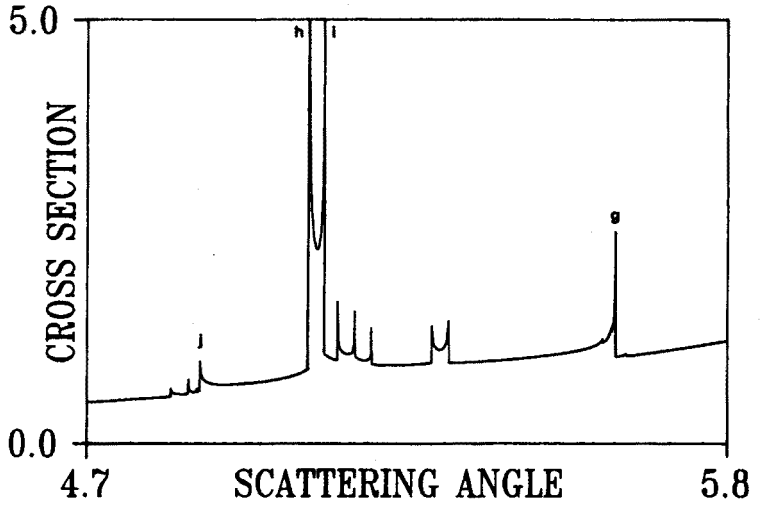

Fig. 10. Classical differential cross section for $E = 0.6$ and $\alpha = \pi$. The four most important rainbows coming from interval R are labelled by lower case letters corresponding to the labels of the deflection function in Fig. 7.

the intervals R, LR, LL, RLL (the most important ones for angle values around $\theta \approx 5\pi/3$) and the background. By background we denote the contributions coming from large initial impact parameter values corresponding to trajectories which pass the potential hills on the outside and do not enter and leave again the potential interior through one of the saddles. Compare the position of the most important rainbow singularities with the positions of the extremal angles in Fig. 9.

Fig. 11 gives the complete cross section. This plot has been produced by the following method; We have started 1600000 trajectories, evenly distributed in the initial impact parameter interval $[-4, +4]$ all with $E = 0.6$ and $\alpha = \pi$. The scattering angle interval $[0, 2\pi)$ has been divided into 3600 boxes and hits of the outgoing asymptotes into the various boxes have been counted. Unfortunately, the resolution is not high. Nevertheless, this plot gives a good impression as to how the contributions from the various intervals are superimposed on the background. Contributions from impact parameter values close to $b = 0$ create the fourfold singularity at angles θ close to π. Compare the deflection function in Fig. 1.

So far the most prominent features of the cross section contributions from the various intervals are the rainbow singularities, especially the nearly degenerate double singularities coming from the middle parts of the intervals. The angular position of these singularities is somewhat different for the various intervals. Next we show that the angular arrangement of these rainbows defines a fractal set with binary organisation, reflecting the frac-

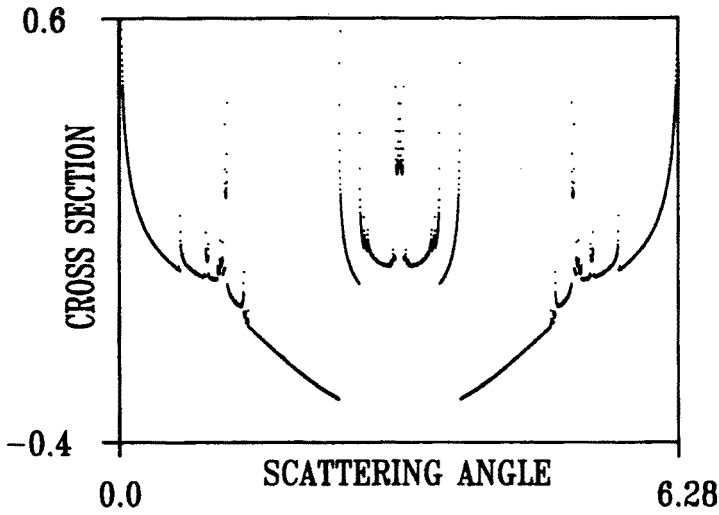

Fig. 11. The complete classical differential cross section for $E = 0.6$ and $\alpha = \pi$. The logarithm of the cross section is plotted as function of the scattering angle.

tal structure of the hyperbolic invariant set in the phase space. To plot Fig. 12 the following has been done; All intervals with signature of length smaller than or equal to 10, and with trajectories going into the angular range around $5\pi/3$, were selected out. For each of these intervals the angular position of the left side of the double singularity (corresponding to point h in Fig. 7) was taken as a characteristic angle and plotted on the angle axis. In the upper frame the various contributions are sorted according to the length of the signature of the corresponding interval. In the lower frame all contributions are plotted along one line. For some contributions the corresponding signature of the interval is shown. Part (b) is a magnification of a small section of part (a) and part (c) is a further magnification.

The binary organisation of the arrangement is evident. Comparison of parts (a), (b) and (c) shows that taking half of the plot and magnifying it is equivalent to shifting the whole structure upwards one step in the signature length. The number of intervals is countable as can be seen from the possibility to label all intervals in closed form by finite signatures. Therefore, also the number of rainbow angles is countable. However, the set of accumulation points of these angles forms an overcountable Cantor set, coinciding with the Cantor set defined by the chaotic saddle in phase space. This can be understood as follows : As the signature of intervals becomes longer and longer by accumulation of new digits in front, the corresponding position space trajectories come closer and closer to the unstable manifold of some localised orbit. In Fig. 9 the spirals of these intervals would converge to the spirals produced by the intersection of the asymptotic θ/L plane with

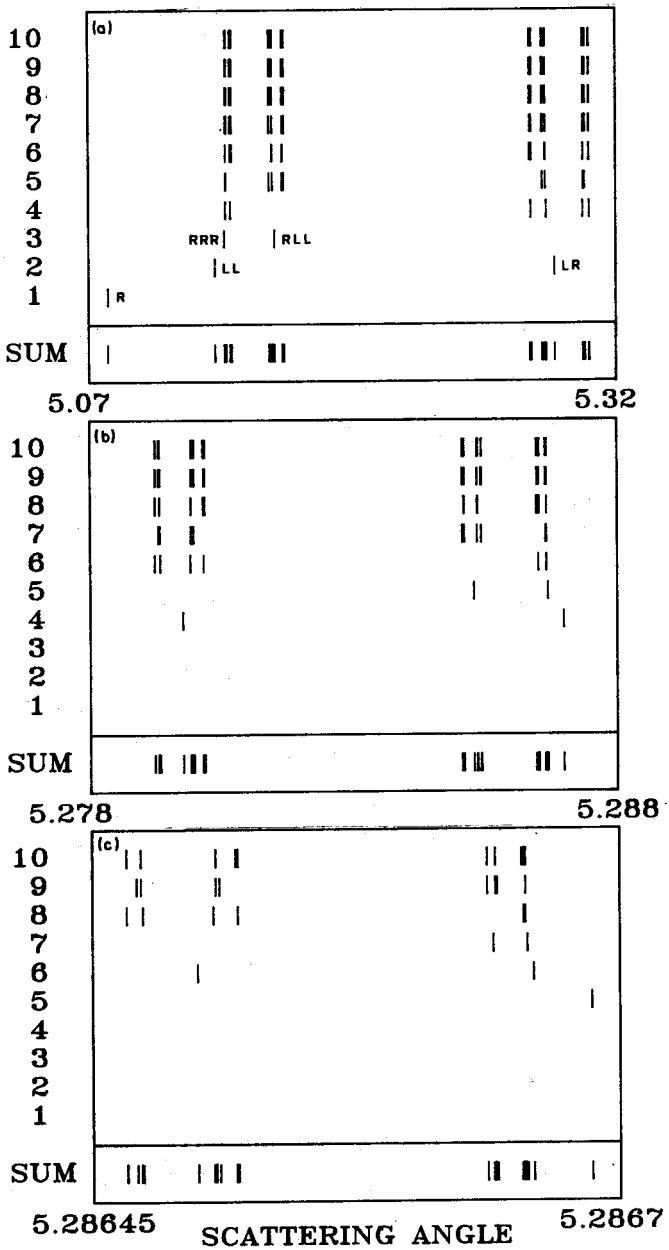

Fig. 12. Fractal pattern of rainbow angles. In the upper frame the contributions from the various intervals are shown as a function of the signature length of the corresponding interval (vertical axis) and the angular position (horizontal axis). In the lower frame the contributions from all signature lengths are plotted along one angular axis. The signatures of the intervals of some contributions are indicated. Part (a) gives an overview over the whole interesting angular interval. Part (b) shows a magnification of an interesting smaller angular interval and part (c) gives a further magnification.

this unstable manifold. Other sequences of intervals would converge against the manifolds of other localised orbits. The whole set of unstable manifolds of all localised orbits gives the fractal structure of the chaotic saddle. Accordingly, the angular minima and maxima of these manifolds are also arranged in this fractal pattern. And the extremal values of the deflection functions of the intervals converge against the extremal values of the angles of the manifolds. Thus, the distribution of the rainbows along the angle axis reflects the fractal pattern of the chaotic set in phase space.

For our numerical examples we always use the angle region around $\theta = 5\pi/3$. In the other two angular regions around $\theta = \pi$ and $\theta = \pi/3$, which are reached by trajectories leaving the potential interior through the other two saddles, the same structure of the cross section can be found. For other values of the incoming direction α nothing changes dramatically as long as there are trajectories entering the potential interior at all, *i.e.* as long as the stable manifolds of the chaotic saddle are intersected by the initial conditions $\vec{p}_{\text{in}} =$ fixed, b arbitrary. Of course, the exact position of the various intervals along the b axis would be shifted. However, when the signature of an interval is sufficiently long, then the corresponding trajectories spend a long time inside the potential region and, in a sense, forget their history. For the shape of the deflection function shown in Fig. 7 all that matters is how the particles leave the potential interior through one of the saddles.

When the value of E is changed, the eigenvalues μ and λ of γ and Γ and the eigenvalues of all other periodic orbits are also changed and the scaling properties of the fractal set changes accordingly. The difference of the values of φ_+ and φ_- in (7) and (8) is the same for all intervals to a very high accuracy. However, the numerical values of $\varphi_+ - \varphi_-$ depend on E. Accordingly the shape of the deflection function in the middle of the intervals, where the asymptotic oscillations from both sides are fitted together, depends strongly on E. We find an exact cubic rainbow at an energy $E_{\text{C}} \approx 0.58$. We have a cubic rainbow at angle θ_{C}, if there is an impact parameter value b_{C} such that $\theta(b_{\text{C}}) = \theta_{\text{C}}$ and $d\theta/db(b_{\text{C}}) = d^2\theta/db^2(b_{\text{C}}) = 0$. At E_{C} the two extrema h and i of the deflection function in Fig. 7 coincide. For $E < E_{\text{C}}$ these two extrema disappear. For E increasing from E_{C} the angular distance between these extrema increases monotonically. The fractal set described here exists as long as $E \in [E_B, E_{\text{M}}]$.

5. Construction of the semiclassical scattering amplitude

So far everything has been described within classical dynamics. However, scattering experiments are an important source of information for micro systems, where quantum effects are essential. Therefore it is important to find the quantum mechanical phenomena which correspond to irregular

scattering in classical mechanics. Because of the limited time, the irregular scattering of waves according to the Schrödinger equation can not be discussed in this lecture. Only a few remarks will be made in the concluding section. Instead, we will restrict ourselves to a semiclassical investigation of the fingerprints of classical scattering chaos in the quantum cross section, since the connections between classical dynamics and quantum dynamics can be investigated within a semiclassical approximation for quantum mechanics. To construct the semiclassical scattering amplitude we shall use Maslov's version of the WKB method [17] which has been cast into a practical form for scattering systems in [18,19].

The first step in this procedure is the construction of the classical Lagrangian submanifold $\mathcal{L}(\vec{p}_{\mathrm{in}})$ belonging to the fixed incoming momentum $\vec{p}_{\mathrm{in}}$. In the position space we choose a straight line $\mathcal{G}$ perpendicular to $\vec{p}_{\mathrm{in}}$ and far away from the origin such that along $\mathcal{G}$ the value of V cannot be distinguished from zero within the computational accuracy. $\mathcal{G}$ is placed on that side of the origin, from which it will be transported towards the potential by the flow. Along $\mathcal{G}$ the impact parameter b is taken as coordinate. The corresponding one-dimensional line $\overline{\mathcal{G}}$ in the four-dimensional phase space is obtained by lifting $\mathcal{G}$ to the constant momentum value $\vec{p}_{\mathrm{in}}$. Next we transport $\overline{\mathcal{G}}$ through the phase space by the flow φ_t of the system. Thereby a two-dimensional submanifold $\mathcal{L}(\vec{p}_{\mathrm{in}})$ is created. For the arbitrary point Q on $\mathcal{L}$ we take w and t as coordinates, where w is the impact parameter with which the trajectory through Q has started, *i.e.*

$$w(Q) = \lim_{t \to -\infty} b(\varphi_t(Q)) \tag{16}$$

and t is the time of flight for the trajectory starting in $(b, 0)$ on $\overline{\mathcal{G}}$ to arrive at Q. The surface $\mathcal{L}$ twists and turns in phase space and grows folds and whirls. By the time it has been transported through the potential interior it lies in an infinite number of branches over the position space.

For scattering systems we are mainly interested in the form of $\mathcal{L}$ in the outgoing asymptotic region. For chaotic scattering systems the mapping from points of $\overline{\mathcal{G}}$ into the outgoing asymptotes has discontinuities on a Cantor set along $\overline{\mathcal{G}}$. Each interval of continuity of b values in between the points of the Cantor set is turned into a spiral shaped whirl during its transport through the potential interior by the flow. In Fig. 9 we have already seen the intersection of the trajectories starting in the intervals R, LR, LL with the asymptotic plane.

In addition to the infinite number of spirals there is one further isolated branch of $\mathcal{L}(\vec{p}_{\mathrm{in}})$ coming from trajectories with large values of b which pass the potential hills on the outside instead of running through the potential interior. The outgoing angular momentum L of these trajectories is ap-

proximately $L \approx 2.5$ for the angular region shown in Fig. 9. Therefore this branch is outside of the frame of Fig. 9.

Later we need the trajectories starting on $\overline{\mathcal{G}}$ and going to a specific outgoing direction $\bar{\theta}$. As an example, the line $\bar{\theta} = 5.4$ is marked by a broken line in Fig. 9. The intersection between $\mathcal{L}$ and the line $\theta = \bar{\theta}$ will be denoted by $D(\bar{\theta})$. Each interval contributes an infinite number of points to $D(\bar{\theta})$ as long as $\bar{\theta}$ is chosen such that the line $\theta = \bar{\theta}$ intersects the set of spirals at all. In this case $D(\bar{\theta})$ is a fractal set.

$\mathcal{L}(\vec{p}_{\text{in}})$ is Lagrangian. Therefore a global action function S exists on $\mathcal{L}$. We define

$$S(w,t) = \int p_x dx + p_y dy = \int \vec{p} \cdot d\vec{q}. \tag{17}$$

The line integral is taken along any path from $(b,0)$ to (w,t) which lies on $\mathcal{L}$. We are dealing with a scattering problem, where the initial point $(b,0)$ and the final point (w,t) are supposed to tend to infinity in position space and we wish to split off the uninteresting motion in the asymptotic region. Accordingly, we define a reduced action $\tilde{S}$ in which the asymptotic parts are split off;

$$\tilde{S}(w,t) = S(w,t) - \vec{p} \cdot \vec{q}|_{\text{final}} + \vec{p} \cdot \vec{q}|_{\text{initial}} = -\int \vec{q} \cdot d\vec{p}. \tag{18}$$

The action $\tilde{S}$ has a definite value for each scattering trajectory independent of the choice of the initial and final point along this trajectory as long as these points are both far away from the potential region. $\tilde{S}$ gives the phase of the contribution of this trajectory to the semiclassical scattering amplitude [20].

Now we give a very brief description of the construction of the semiclassical wave function and scattering amplitude. The method is presented in full detail in [17-19]. On $\mathcal{L}(\vec{p}_{\text{in}})$ we define a density

$$\rho(w,t) = \frac{\rho_{\text{in}}(b)}{J(w,t)} \tag{19}$$

with

$$J(w,t) = \det \frac{\partial q(w,t)}{\partial(w,t)}, \tag{20}$$

where $q(w,t)$ is the position space point onto which (w,t) projects. ρ_{in} is an incoming density on $\mathcal{G}$ which is supposed to be constant for our boundary conditions. On each open subset of $\mathcal{L}(\vec{p}_{\text{in}})$, which projects one-to-one into the position space we construct the wave function

$$\chi(w,t) = \rho(w,t)^{1/2} \exp\left[\frac{iS(w,t)}{\hbar} - \frac{i\pi\mu}{2}\right], \tag{21}$$

where μ is the Maslov index of the trajectory from $(b,0)$ to (w,t). In our system it coincides with the number of caustics of $\mathcal{L}(\vec{p}_{\text{in}})$ crossed by this trajectory. In general $\mathcal{L}$ lies in many sheets over the position space and the semiclassical Schrödinger wave function $\psi(x,y)$ in configuration space is obtained by summation of χ over all the branches of $\mathcal{L}$ lying over (x,y), *i.e.*

$$\psi(x,y) = \sum_j \rho_j(w_j,t_j)^{1/2} \exp\left[\frac{iS_j(w_j,t_j)}{\hbar} - \frac{i\pi\mu}{2}\right], \tag{22}$$

where (w_j,t_j) projects onto (x,y) for all j.

Along caustics $\mathcal{L}$ does not project one-to-one into the position space and the density ρ in Eq. (19) diverges. Then the form of the wave function in (21) and (22) is not a usefull semiclassical approximation. Near caustics $\mathcal{L}$ projects one-to-one into the momentum space and we can construct an approximation for the momentum space wave function in terms of the exponential functions. Then we Fourier transform this non-singular momentum space wave function in order to obtain a non-singular position space wave function. By a smooth monotonic transformation of the integration variable the Fourier integral can be transformed into an appropriate normal form. It is the integral over a product of a slowly varying amplitude function times the exponential function of a polynomial. If the caustic is an isolated fold of $\mathcal{L}$, then we need a polynomial of order three and the integral gives a combination of an Airy function and its derivative. If the caustic is a cusp or two neighbouring folds which are not well separated, then we need a polynomial of order four and the integral gives a combination of a Pearcy function and its derivatives. More complicated caustics do not occur in system (1).

The Airy and Pearcy contributions from the surroundings of caustics have to be joined smoothly to the exponential functions from regions far away from caustics. This is done by appropriate partitions of unity on $\mathcal{L}$. The theory of this switching between position and momentum space is presented in mathematically rigorous form in [17].

In the outgoing asymptotic region we separate the function (22) into a radial and an angular part. ρ splits as

$$\rho = r^{-1}\left|\frac{d\theta}{db}(b_j)\right|^{-1} \tag{23}$$

and from S we add the asymptotic radial contribution $\vec{q}_{\text{in}}\cdot\vec{p}_{\text{in}}$ and subtract $\vec{q}_{\text{out}}\cdot\vec{p}_{\text{out}}$ giving $\tilde{S}$, already introduced in (18). For the signs in (18) note that $\vec{q}_{\text{in}}$ and $\vec{p}_{\text{in}}$ point in opposite directions whereas $\vec{q}_{\text{out}}$ and $\vec{p}_{\text{out}}$ point in the same direction. In the limit $r\to\infty$ we have $-\vec{q}_{\text{in}}\cdot\vec{p}_{\text{in}} = r_{\text{in}}k$ and $\vec{q}_{\text{out}}\cdot\vec{p}_{\text{out}} = r_{\text{out}}k$ where $k=\sqrt{2E}$. So we can split off the same radial factor $r^{-1/2}\exp[ik(r_{\text{in}}+r_{\text{out}})]$ from each term in (22). The remaining angular

factor of the wave function in the outgoing asymptotic region is just the semiclassical scattering amplitude. We obtain the well known expression [20];

$$f(\theta) = \sum_j \sqrt{c_j} \exp\left[\frac{i\tilde{S}_j(\theta)}{\hbar} - \frac{i\pi\mu_j}{2}\right], \tag{24}$$

where

$$c_j = \left|\frac{d\theta}{db}(b_j)\right|^{-1} \tag{25}$$

is the contribution of trajectory j to the classical cross section. The sum runs over all classical trajectories starting with incoming momentum $\vec{p}_{\text{in}}$ and going out with scattering angle θ. Also in (24) we need an uniformisation close to caustics. It is induced by the uniformisation of the wave function. The differential cross section is given by

$$\frac{d\sigma}{d\theta}(\theta) = |f(\theta)|^2. \tag{26}$$

For many systems and in particular for chaotic bound systems the semiclassical sums like the one in (24) do not converge absolutely. However, for many scattering systems, and especially for energies not too small, the semiclassical sum for the amplitude converges absolutely. Next let us give a brief estimate of the convergence properties for the sum (24). First consider the sum over the contributions from one particular interval, *e.g.* interval R shown in Fig. 7. For any particular value of the angle θ we group these contributions into four classes. For example of $\theta = 5.4$ shown in Fig. 7 by a broken line, class 1 contains the points B, F, J, *etc.* Class 2 contains C, G, K, *etc.* Class 3 contains A, E, I, *etc.* Class 4 contains D, H, L, *etc.* Any class contains a sequence of second next neighbouring points running towards one boundary of the interval and leading to a given value of θ. Going from one contribution of any class to the next one of the same class, the weight $\sqrt{c_j}$ of the contribution decreases by a factor $\sqrt{\mu}$ in the limit of close approach to the boundary. The eigenvalue μ of the trajectory γ is always greater than 1 since γ is unstable

$$c_{k+1,l} \approx \frac{c_{k,l}}{\mu}, \tag{27}$$

where $c_{k,l}$ is the classical weight of the k-th member of class l. For the sum of all contributions from interval R we find an estimate by a geometrical series

$$|f_R| \leq \sum_{l=1}^{4} \sum_{k=0}^{\infty} \sqrt{c_{k,l}} \approx \sum_{l=1}^{4} \sqrt{c_{0,l}} \sum_{k=0}^{\infty} \mu^{-k/2} \tag{28}$$

Next we have to estimate the sum over all intervals. All intervals give similar sequences of contributions, the only difference being that the corresponding weights c_j are scaled proportional to the total length of the interval. Let us group the intervals into various generations where the generation number is given by the length of the signature of the intervals. There are 2^N intervals of generation N. The ratio of the length of any interval compared to the length of its neighbouring interval of the next generation is always between $\mu^{1/2}$ and $(-\lambda)^{1/3}$. Therefore, the weights $\sqrt{c_j}$ of the contributions to sum (24) of any interval are decreased by a factor of at least $(-\lambda)^{1/6}$ compared to the corresponding weights of the neighbouring interval of the next generation. Let n be an index which numbers the 2^N intervals of generation N and let $f_{n,N}$ be the contribution of interval n of generation N to the sum (24). According to what has been explained so far, we find

$$|f_{n,N}| \leq |\lambda|^{-N/6} |f_{1,1}|, \tag{29}$$

for any n and N. For the total amplitude we find the estimate

$$|f| \leq \sum_{N=1}^{\infty} \sum_{n=1}^{2^N} |f_{n,N}| \leq \sum_{N=1}^{\infty} 2^N |\lambda|^{-N/6} |f_{1,1}|. \tag{30}$$

This sum converges, if $|\lambda| > 2^6 = 64$ which is fulfilled for $E > 0.58$.

The estimates used in (29) and (30) are very rough since we have always inserted the largest scaling factor which can occur at all. A more careful estimate using the average scaling factor indicates that we may expect absolute convergence for energies as low as 0.52. However, for energies close to E_S there is definitely no absolute convergence of the semiclassical sum (24). Also for most other chaotic scattering systems we expect energy intervals to exist, in which the semiclassical sum is not absolutely convergent. In these cases an appropriate resummation has to be applied which might be constructed along the pattern of rearrangement of semiclassical series mentioned in [21].

In case of absolute convergence we can set a limit of accuracy and take only a finite number of branches of $\mathcal{L}$ into account which are needed in order to stay within the given limit of accuracy. In the following we are mainly interested in qualitative results and for this purpose it is sufficient to take the following branches of $\mathcal{L}$, which give the most important contributions for angle values around $\theta = 5\pi/3$. From each of the intervals R, LR, LL, RLL we take the nine most important branches respectively. In addition we take the isolated branch from trajectories not entering the potential interior. This branch gives the strongest contribution of all. In the following we call the contribution from this outer branch the background.

6. The semiclassical cross section

The most prominent structure in the classical cross section caused by the existence of chaos is the fractal pattern of rainbow singularities. Therefore, we now look which part of this structure survive in the semiclassical cross section depending on the value of $\hbar$.

Fig. 13 gives the semiclassical cross section in the angle interval $\theta \in [4.7, 5.8]$ for $\hbar = 0.005$. The arrows in this Fig. indicate the angular positions of the most important rainbows coming from contributions of interval R and their labels match the ones of Figs 7 and 10. An interesting property of $d\sigma/d\theta$ is the destructive interference between several caustic contributions near $\theta = 4.9$. For $\hbar = 0.005$ the various caustics are not well separated along the θ axis and we have many overlapping rainbows. This causes an effect which reminds of the anticaustic effect (decreased amplitude of the wave function at the position of clusters of caustics) mentioned in [22]. Comparison between Fig. 10 and Fig. 13 makes evident that at $\hbar = 0.005$ the rainbows are not well resolved in the semiclassical cross section. So let us decrease the value of $\hbar$.

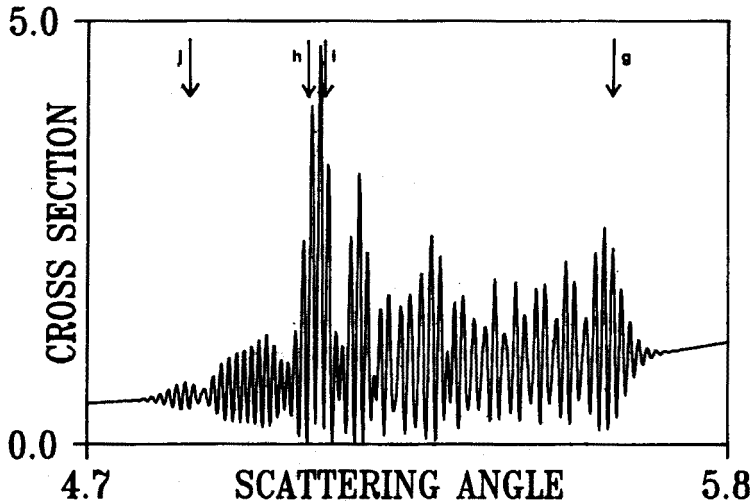

Fig. 13. Semiclassical cross section in the angular interval $\theta \in [4.7, 5.8]$ for $\hbar = 0.005, E = 0.6$ and $\alpha = \pi$.

Fig. 14 gives the semiclassical cross section in the angular interval $\theta \in [4.86, 4.91]$ for $\hbar = 0.0001$. Now the rainbow j from interval R is clearly resolved. The other arrow without label gives the position of that rainbow coming from interval RL, which corresponds to rainbow j from interval

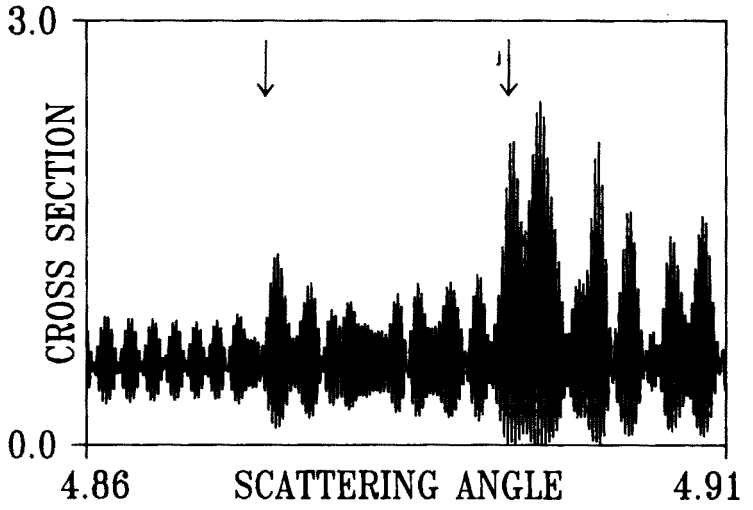

Fig. 14. Semiclassical cross section in the angular interval $\theta \in [4.86, 4.91]$ for $\hbar = 0.0001, E = 0.6$ and $\alpha = \pi$.

R. These two rainbows are now clearly separated. Also the shape of the cross section in the angular region containing the double singularity h and i changes drastically for smaller values of $\hbar$. Fig. 15 shows the semiclassical cross section in the angular interval $\theta \in [5.07, 5.12]$ for $\hbar = 0.0001$. Now the two rainbows h and i are clearly separated. In Fig. 16 we give the semiclassical cross section in the angular interval $\theta \in [4.8925, 4.894]$ for $\hbar = 10^{-6}$. In this Fig. the fast interference oscillations with the background are not resolved. However, they are of the same qualitative structure as before, only compressed proportionally to the vale of $\hbar$. The envelope curve of the rainbow structure clearly reminds us of a classical rainbow at $\theta = \theta_R$ with a shape like $(\theta - \theta_R)^{-1/2}$ on the illuminated side.

In the limit of small $\hbar$ the semiclassical cross section reproduces the classical cross section in the following way: the semiclassical cross section contains fast interference oscillations between the contributions from the various branches of $\mathcal{L}$. The wavelength of these oscillations along the θ axis scales like $\hbar$. In addition, close to caustics there exist oscillations coming from the Airy function contributions. The width of the main peak of the Airy function is proportional to $\hbar^{2/3}$ and its height grows like $\hbar^{-1/3}$ in the limit of small $\hbar$. In this way sharp peaks of the cross section emerge in the limit of small $\hbar$ at the positions of the classical rainbows, which are located in a fractal arrangement. If we continue to decrease $\hbar$, then more and more smaller rainbows emerge and become well separated from neighbouring rainbows. To reproduce the classical cross section, let us average

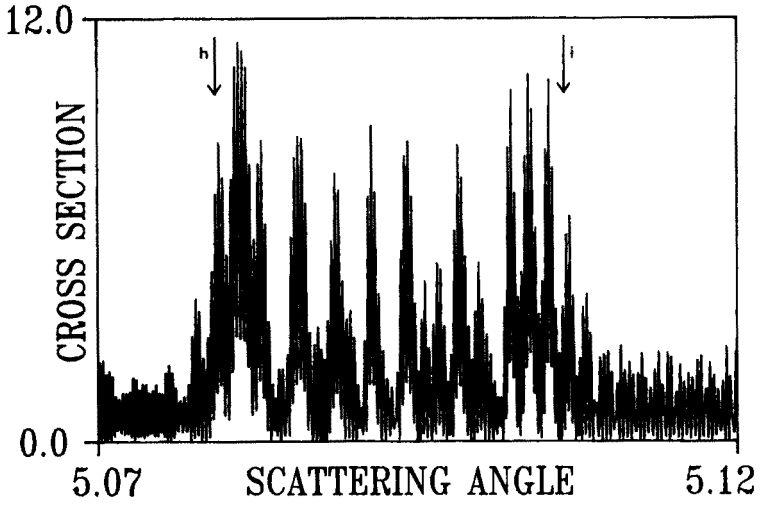

Fig. 15. Semiclassical cross section in the angular interval $\theta \in [5.07, 5.12]$ for $\hbar = 0.0001$, $E = 0.6$ and $\alpha = \pi$.

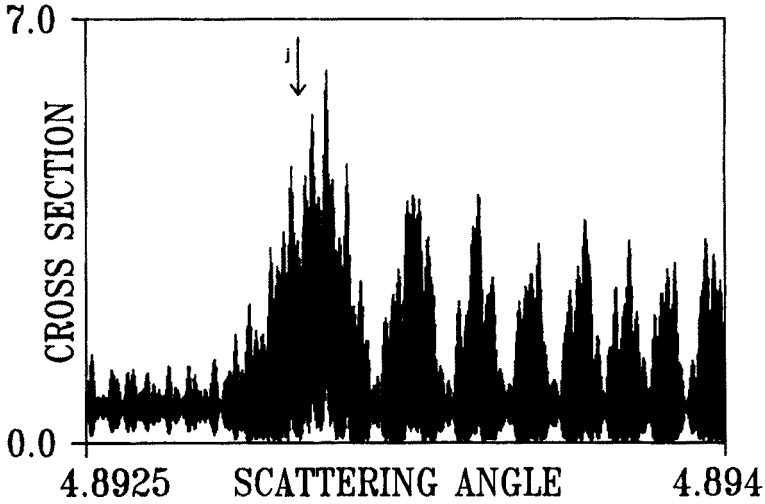

Fig. 16. Semiclassical cross section in the angular interval $\theta \in [4.8925, 4.894]$ for $\hbar = 10^{-6}$, $E = 0.6$ and $\alpha = \pi$.

the semiclassical cross section for a particular value of $\hbar$ according to

$$\left\langle \frac{d\sigma}{d\theta}(\theta) \right\rangle = \frac{1}{2c} \int_{\theta-c}^{\theta+c} \frac{d\sigma}{d\theta}(\hat{\theta}) d\hat{\theta}. \tag{31}$$

We choose $2c$, the length of the averaging interval, proportional to $\hbar^{1/2}$ such that in the limit $\hbar \to 0$ the number of interference oscillations in the integration interval grows without limit. Also the width of the Airy peaks becomes small compared to the averaging length. When we let $\hbar$ tend to 0 in $d\sigma/d\theta$ and in c simultaneously, then $\langle d\sigma/d\theta \rangle$ approaches the classical cross section.

Because we have seen that it is not so easy to extract the rainbow pattern from the semiclassical cross section, we now try out another idea to extract information on the classical chaos and the fractal structure from the semiclassical cross section. The most spectacular difference between the classical and the semiclassical cross section are the interference oscillations in the semiclassical cross section. Therefore, let us now try to evaluate the pattern of oscillation frequencies in the semiclassical cross section.

We pick out a θ interval $I = [\bar{\theta}, \bar{\theta} + \Delta\theta]$ away from all classical rainbow singularities. Then $d\theta/db(b_j) \neq 0$ for all j and all $\theta \in I$, the number of solutions of $b(\theta)$ does not change inside I and c_j varies only slowly inside I along any branch of $\mathcal{L}$ and we approximate

$$c_j(\theta) = \left| \frac{d\theta}{db}(b_j(\theta)) \right|^{-1} = c_j(\bar{\theta}). \tag{32}$$

$\tilde{S}(\theta)$ is expanded up to first order around $\bar{\theta}$ as

$$\tilde{S}_j(\theta) = \tilde{S}_j(\bar{\theta}) + (\theta - \bar{\theta}) \frac{d\tilde{S}_j}{d\theta}(\bar{\theta}), \tag{33}$$

where $d\tilde{S}_j/d\theta(\bar{\theta}) = L_j(\bar{\theta})$ is the outgoing angular momentum of trajectory j. Using the notation

$$\varphi_j = \frac{[\tilde{S}_j(\bar{\theta}) - \bar{\theta} L_j]}{\hbar} - \frac{\mu_j \pi}{2}, \tag{34}$$

we obtain

$$f(\theta) = \sum_j \sqrt{c_j} \exp(i\varphi_j) \exp(i\theta L_j/\hbar), \tag{35}$$

f is the Fourier transform of

$$F(L) = \sum_j \sqrt{c_j} \exp(i\varphi_j) \delta(L - L_j). \tag{36}$$

The support of F is the classical fractal set $D(\bar{\theta})$. For the cross section we obtain

$$\frac{d\sigma}{d\theta}(\theta) = \sum_j c_j + \sum_{k<j} \sqrt{c_j c_k} 2 \cos\left(\varphi_k - \varphi_j + \frac{\theta(L_k - L_j)}{\hbar}\right). \qquad (37)$$

The frequencies occuring in the interference terms are given by $(L_k - L_j)/\hbar$; they also form a fractal distribution.

Let us illustrate this behaviour by an example for system (1) and $\bar{\theta} = 5.4, E = 0.6, \alpha = \pi$; Fig. 17 shows the position of the most important values of $L_k - L_j$ (in linear scale on the horizontal axis) and the corresponding values of the logarithms of the weights $\sqrt{c_k c_j}$. Parts (b) and (c) are magnifications which illustrate the fractal character of the set of angular momentum differences.

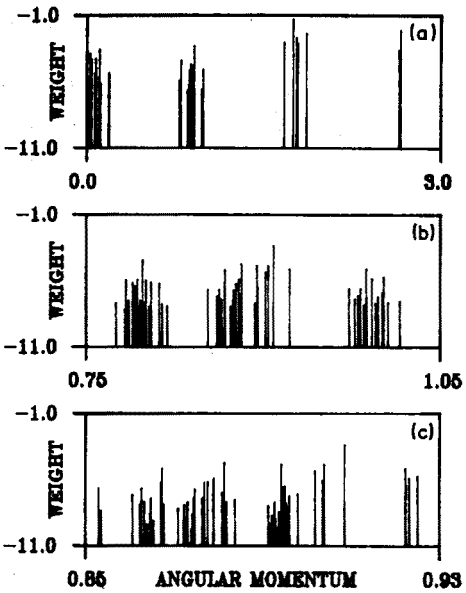

Fig. 17. Plot of $\ln \sqrt{c_k c_j}$ (vertical axis) as a function of $L_k - L_j$ (horizontal axis). The 9,17 and 32 most important branches of $\mathcal{L}$ have been taken into account in parts (a),(b) and (c) respectively. $E = 0.6, \alpha = \pi$.

Fig. 18 shows the semiclassical cross section for a small interval of scattering angles. In part (a) $\hbar = 10^{-5}$ and in part (b) $\hbar = 10^{-6}$. In the semiclassical sum the 32 most important contributions have been taken into account. In part (b) the fast fluctuations are not resolved, they are of

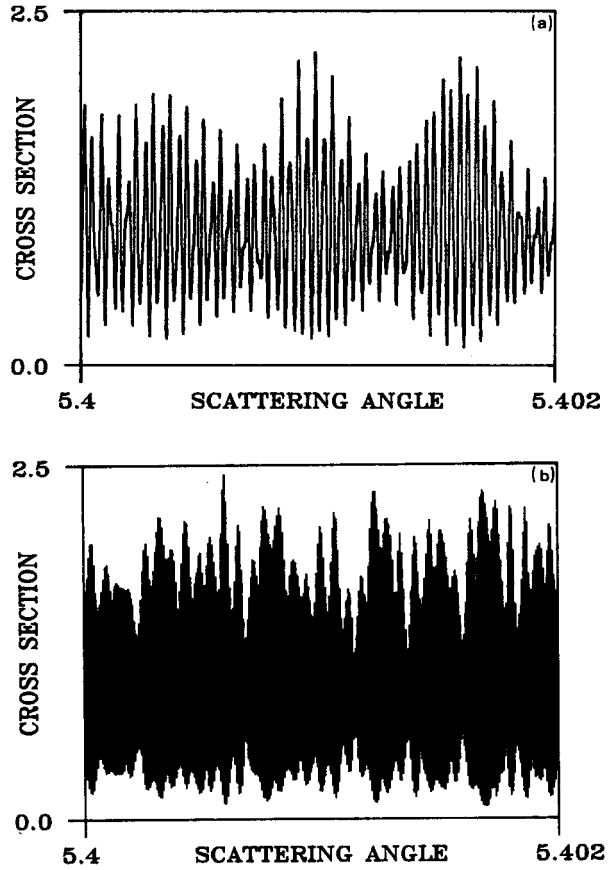

Fig. 18. Semiclassical cross section as a function of the scattering angle for $E = 0.6, \alpha = \pi$. $\hbar = 10^{-5}$ in part (a) and $\hbar = 10^{-6}$ in part (b).

the same qualitative structure as in part (a) only compressed by a factor of 10.

Fig. 19 shows the Fourier transform of the cross section from Fig. 18 (a). Comparison with Fig. 17 shows in which way the interference frequencies give the pattern of angular momentum differences and therefore also the classical fractal structure.

Next let us estimate the error we make, when we reconstruct the fractal set $D(\theta)$ from the data of $d\sigma/d\theta(\theta)$. By taking a Fourier transform of $d\sigma/d\theta(\theta)$ over θ in the interval I of length $\Delta\theta$, we do not get sharp values of L. Instead, for each contributing L value we obtain a broadened peak. The width of these peaks comes from two sources. First, the finite length $\Delta\theta$ of the interval I causes a width $\Delta_1 = 2\pi\hbar/\Delta\theta$. Second, the nonlinear terms omitted in expansion (33) create a further broadening. Expansion (33) only

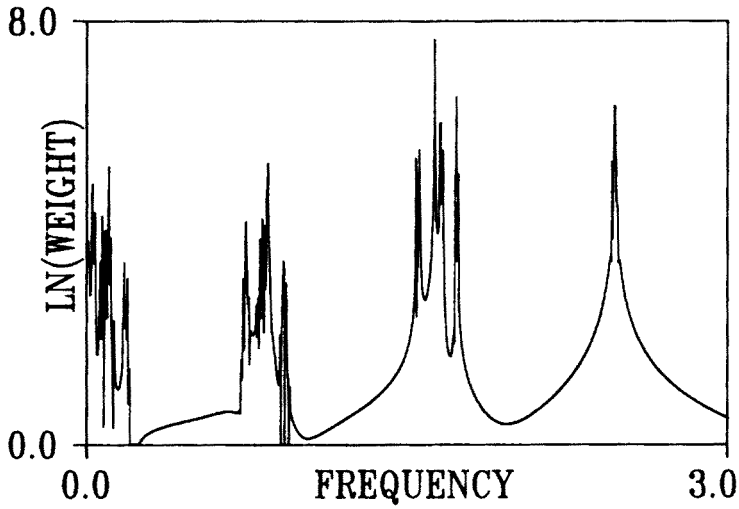

Fig. 19. Logarithm of the Fourier transform of the semiclassical cross section shown in Fig. 18 (b).

makes sense if L_j is sufficiently constant inside the interval I along each branch of $\mathcal{L}$. Choose δ such that

$$\left|\frac{d^2 S_j(\theta)}{d\theta^2}\right| = \left|\frac{dL_j}{d\theta}\right| < \delta \tag{38}$$

for all j and all $\theta \in I$. Then $|L_j(\theta) - L_j(\bar{\theta})| < \delta\Delta\theta = \Delta_2$. And the broadening of the L values due to the nonlinearity of $S_j(\theta)$ is at most Δ_2. For given values of $\hbar$ and $\Delta\theta$ we can expect to resolve $D(\bar{\theta})$ to an accuracy of $\Delta = \Delta_1 + \Delta_2$. When we make $\hbar$ smaller and smaller we let $\Delta\theta$ decrease like $\hbar^{1/2}$. Then Δ_1 and Δ_2 both decrease like $\hbar^{1/2}$. By repeating the procedure for various values of $\bar{\theta}$ we can reconstruct the classical Lagrangian submanifold $\mathcal{L}(\vec{p}_{\text{in}})$ with an accuracy $\Delta \propto \hbar^{1/2}$. In total, we have pulled a classical fractal set out of a quantum mechanical observable quantity, at least approximately in the limit of small $\hbar$.

So far we have investigated the cross section as a function of the scattering angle for fixed energy. We can also obtain useful information, when we look at the cross section as a function of the energy for fixed scattering angle. Next we give a few remarks on these possibilities. In analogy to what we have done before, we start by expanding the reduced action as function of the energy around some reference value E_0 of the energy:

$$\tilde{S}_j(E) = \tilde{S}_j(E_0) + (E - E_0)\frac{\partial \tilde{S}_j}{\partial E}(E_0), \tag{39}$$

where $T_j = \partial \tilde{S}_j / \partial E$ is the time delay of trajectory j in the potential interior. The derivative in (39) is done for fixed incoming direction α and fixed scattering angle θ. Compared to $\tilde{S}(E)/\hbar$ the quantities c_j and T_j are slowly varying as function of E in the limit of small $\hbar$ and they will be replaced by their value at E_0. With the abbreviation

$$\eta_j = -\frac{E_0 T_j(E_0)}{\hbar} + \frac{\tilde{S}_j(E_0)}{\hbar} - \frac{\pi \mu_j}{2}, \tag{40}$$

the amplitude in (24) becomes

$$f(E) = \sum_j \sqrt{c_j} \exp(i\eta_j) \exp\left(\frac{iET_j}{\hbar}\right) \tag{41}$$

and the cross section is

$$\frac{d\sigma}{d\theta}(E) = \sum_j c_j + \sum_{j<k} \sqrt{c_j c_k} 2 \cos[\eta_j - \eta_k + E(T_j - T_k)/\hbar]. \tag{42}$$

The first sum in (42) is the classical cross section. The second double sum represents the quantum mechanical interference terms. Their oscillation frequencies are given by

$$\Omega_{j,k} = (T_j - T_k)/\hbar. \tag{43}$$

The set of accumulation points of the set of Ω values forms a fractal pattern.

To visualize this, we choose $\theta = 5.4$ and $E = 0.6$ and pick out from each interval the two trajectories corresponding to the points B and C in Fig. 7 for interval R. In Fig. 20 we show a plot of the time delay differences obtained in this way. The horizontal axis gives the time delay differences. The vertical axis gives the generation number. Some contributions are labelled with the signature of their interval. This plot has exactly the same structure as the fractal arrangement of rainbows shown in Fig. 12 (a). This structure reflects the arrangement of the unstable manifolds of the chaotic saddle in the classical phase space.

In the cross section in Eq. (42) there are not only interference terms between the contributions B and C within each interval. In addition, there are interferences between any two terms in the semiclassical sum (42). The set of all occuring differences of time delays is a very complicated fractal structure containing an infinite number of shifted copies of the structure shown in Fig. 20.

Fig. 21 gives an example of $d\sigma/d\theta(E)$ for our model system (1). $\hbar = 10^{-5}$ in part (a) and $\hbar = 10^{-6}$ in part (b). The energy interval displayed is

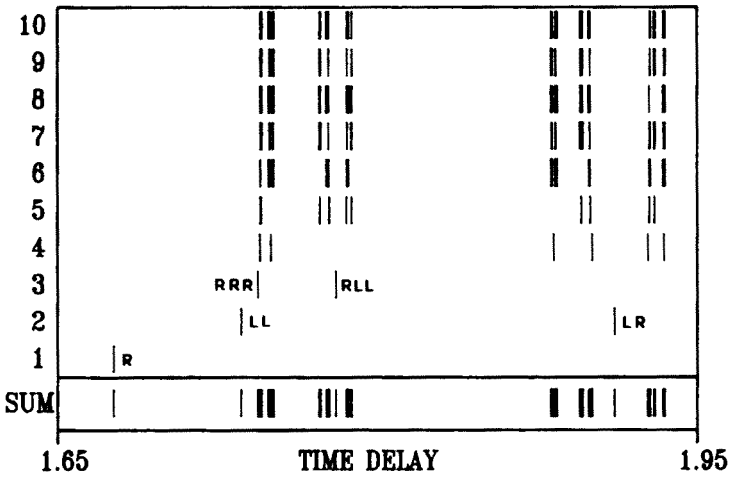

Fig. 20. Difference of the time delays T_B and T_C for the intervals of generations 1-10. In the upper frame the contributions are sorted according to the generation number of the intervals. In the lower frame all contributions are accumulated.

$E \in [0.6, 0.6005]$ and $\theta = 5.4$ which is far away from all classical rainbows. We have taken into account the 32 most important branches of $\mathcal{L}$. In part (b) the fast oscillations are not well resolved. They are of the same qualitative structure as in part (a), only compressed by a factor 10. From part (b) we get an impression of the fluctuations on all scales which $d\sigma/d\theta(E)$ shows in the limit of small $\hbar$. If the function $d\sigma/d\theta(E)$ is given inside an appropriate interval of E values , then we can apply a local Fourier transformation to this function in order to recover an approximate picture of the distribution of time delays. For the resolution of this procedure we find estimates in complete analogy to the ones given above for the case of $d\sigma/d\theta$ as function of θ.

Fig. 22 shows the Fourier transform of the cross section shown in Fig. 21 (a). Each peak of this plot corresponds to one particular combination of two trajectories which contribute to the semiclassical sum (24). For large values of T the slope of the envelope of the curve is approximately -0.4, giving the value of the escape rate $\kappa \approx 0.4$ of the chaotic saddle. In the limit of trajectories spending a long time inside the potential interior the relative probability $P(T)$ to find a trajectory with time delay T is given by

$$P(T) = \kappa \exp(-\kappa T). \tag{44}$$

For more information on this see the lecture by T. Tel and [14].

Let us close with a remark on the relation of this result to the ones presented in [7,23,24]. There the energy correlation function of the quantum mechanical scattering amplitude has been evaluated. Its computation

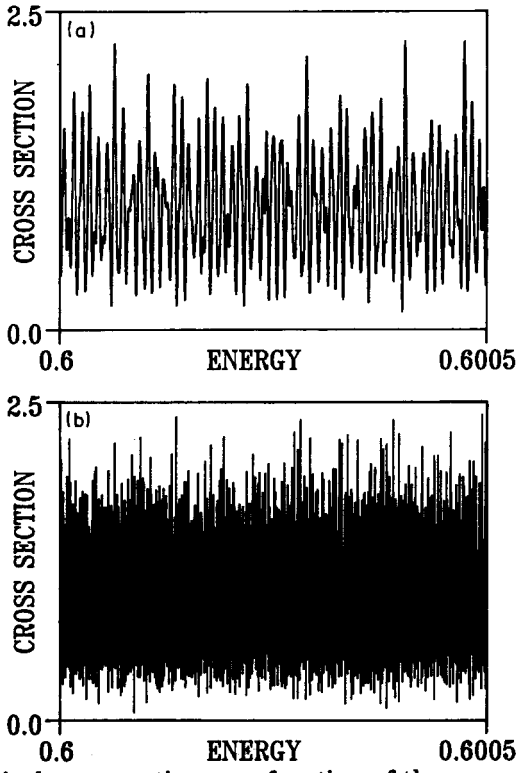

Fig. 21. Semiclassical cross section as a function of the energy for $\theta = 5.4, \alpha = \pi$. $\hbar = 10^{-5}$ in part (a) and $\hbar = 10^{-6}$ in part (b).

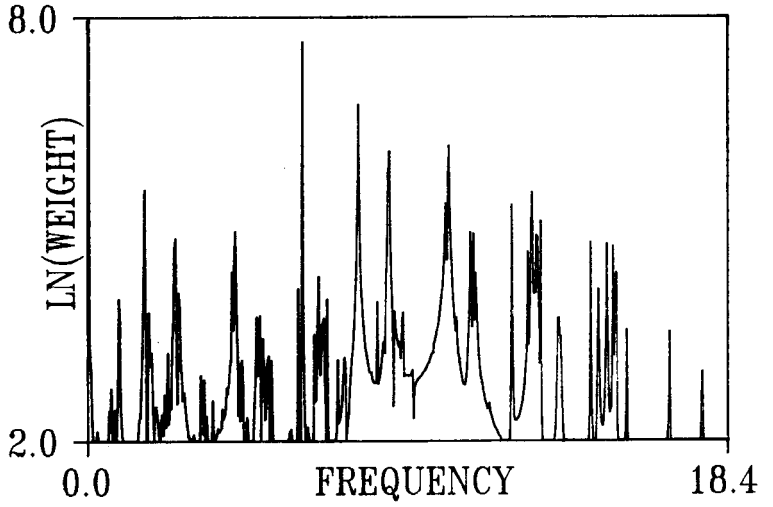

Fig. 22. Logarithm of the Fourier transform of the semiclassical cross section shown in Fig. 20 (b).

contains an averaging process over small energy intervals. Thereby, the knowledge about the fine detailed structure of the chaos is lost. Consequently, as an essential measure of the classical chaotic saddle the escape rate κ can be extracted out of the quantum mechanical scattering amplitude. On the other hand, the procedure of [7,23,24] gives useful results also in those cases in which $\hbar$ (the variable value of $\hbar$ in model computations corresponds to the ratio between the wavelength of the incoming projectile and the effective diameter of the target in real systems) is not as extremely small as the value which we have used in our numerical examples.

7. Final remarks

In this lecture we have learned some properties of the model system (1) for chaotic scattering. Of course, in the end we are interested to know what in system (1) is typical and what is not typical for the general situation in scattering chaos. In any system showing classiacal scattering chaos there is a localised chaotic invariant set in phase space, a so called chaotic saddle. The genuine scattering trajectories are not chaotic themselves, but they come close to the chaotic saddle, move alongside the chaotic localised orbits for a while and transport the information about the chaotic saddle with them into the outgoing asymptotic region. This is a typical example for transient chaos. From the behaviour of the scattering trajectories we can reconstruct all important quantitative measures of the chaotic saddle (see [16]). One property of system (1) which is not typical for all chaotic scattering systems is the global exact and complete binary signature. In general there may be elliptic orbits and surrounding KAM tori in phase space and this prevents the construction of an globally exact symbolic dynamics. Otherwise, our model system (1) provides a typical example for the properties of scattering chaos and for the methods which can be used in order to investigate it. The most important intention of section 6 was to find some fingerprints of classical chaos in the semiclassical scattering cross section. The main result in this respect is the following: the scattering cross section has a fractal cluster of rainbows and shows oscillations on all scales in the limit of small $\hbar$. This is consistent with the predictions of the same properties for semiclassical chaotic wave functions given in [25]. We look at a system in the asymptotic range, where the radial degree of freedom is uninteresting and has been separated off. Therefore only one essential degree of freedom, the angle, remains. If we look at our construction from a more abstract point of view, we can characterise it like this: given is a two-dimensional phase space with canonical coordinates θ and L and in it the Lagrangian submanifold $\mathcal{L}$, given by the spirals shown in Fig. 9. Along $\mathcal{L}$ the action function $\tilde{S}$ and the Maslov index μ are given. We construct the semiclassical wave function

$f(\theta)$ for this Lagrangian submanifold according to the rules of Maslov. Of course, a structure like $\mathcal{L}$ shown in Fig. 9 could never be the Lagrangian submanifold for an autonomous system with one degree of freedom and a smooth Hamiltonian function. In those systems the invariant Lagrangian submanifolds — which are the curves H = constant — are homeomorphic to lines and/or circles but never to a fractal arrangement of spirals. However, in non-autonomous systems the Lagrangian submanifolds can grow infinite whirls and clusters of caustics, which come close to our spirals (see the figures in [25]). Accordingly, in our scattering amplitude, which is constructed like a one-dimensional wave function to a non-autonomous system, we see phenomena of the type which have been observed in wave functions of one-dimensional non-autonomous chaotic systems.

By a careful study of the caustic positions and of the frequency spectra of the interference oscillations we can recover classical fractal sets out of the quantum cross section in the limit of small $\hbar$. Because $\hbar = 0$ is an essential singularity of quantum mechanics, we can not take the value $\hbar = 0$ itself in an investigation of semiclassical quantities. We can only go to smaller and smaller values of $\hbar$ and see the images of classical fractal structures being resolved better and better on more and more levels of the infinite hierarchy of levels. But, it is not possible to have the classical fractals resolved on all infinite levels simultaneously.

In our considerations of the semiclassics we have only followed one very direct way of investigation starting from the amplitude (24) and concentrating on fractal structures. There is another promising way: the trace of the Green's function for the Schrödinger equation can be expressed semiclassically in terms of the periodic orbits of the corresponding classical system [26]. The quantum S-matrix is essentially determined by its poles in the complex energy plane and they coincide with the poles of the Green's function. Thereby the structure of the set of classical periodic orbits determines the semiclassical S-matrix and also the semiclassical scattering amplitude and cross section. For some steps in this direction see [21] and [27].

In all our considerations we have assumed, that the incoming direction of the projectile relative to the target is kept fixed. For real scattering experiments this usually requires that the orientation of the target is fixed in space. Otherwise all interference oscillations are averaged out. Usually this condition is not fulfilled in the scattering of two microscopic particles off each other. However, it is fulfilled in the scattering of a particle off a macroscopic target, *e.g.* the scattering of an electron off electrically charged objects. It is also fulfilled for the motion of ballistic electrons in mesoscopic semiconductors. In this case the motion is essentially two-dimensional and, therefore, it comes even closer to the case considered in this lecture. Interestingly, the chaotic fluctuation of the conductivity of small semiconductors

has recently been interpreted in terms of chaotic scattering [28,29].

The problem of the orientation of the target can also be avoided, if we use a system which is essentially 1-dimensional and make it explicitely time dependent, *e.g.* if we place it into an external oscillating field. As an example for such a situation, the field modified scattering of a particle in the 1-dimensional Morse potential has been analysed in [30]. Because of the analogy between time dependent systems with n degrees of freedom and time independent systems with $n+1$ degrees of freedom, all the methods explained in this lecture can also be applied with only very small modifications to time dependent scattering systems.

Finally, let us make a few remarks on irregular wave scattering; In quantum mechanics the central object of scattering theory is the S matrix. In analogy to the quantisation of bound systems, where classical chaos is correlated with random matrix properties of the wave dynamics, the followin hypothesis has been formulated for quantum scattering [7,23,24]; The statistical properties of the S matrix (for $\hbar \to 0$) are determined by Dyson's theory for the orthogonal ensemble of random unitary matrices. As an example for this statement in [31] the scattering of an incoming wave off an infinite array of scattering centers placed along a line has been investigated in detail and compared to the classical properties of the same system, which have been worked out in [32]. These statements have also been checked by microwave reflection from a cavity [33] and by transmission of microwaves through junctions [34]. Because of the macroscopic nature of microwaves, the measurement of phases and not only of intensities of the wave is possible in contrast to quantum mechanics.

For the scattering off three hard discs the wave dynamics has been presented in [35] and compared to the corresponding semiclassical computations presented in [27].

In [36] the statistical distribution of the location of the poles (resonances) of the S matrix in the complexe energy plane has been described for irregular wave scattering by the Ginibre ensemble.

In [37] the wave scattering on a surface of negative curvature has been investigated by analytical methods. The phase shift could be expressed by a Riemann ζ function, which represents a chaotic function.

In total, the connection between random matrix behaviour in quantum scattering and classical scattering chaos (= Cantor set of singularities in the deflection function, chaotic saddle in the phase space) is not yet completely clear. As has been pointed out in [38], the quantum S matrix is also expected to have eigenvalues (eigenphases) according to the Circular Orthogonal Ensemble and probably also some further random matrix properties, whenever there is no real classical scattering chaos but only chaos in the classical iterated scattering map, whose construction has been worked

out in [39-41]. Unfortunately, the meaning of this result is unclear at the moment.

REFERENCES

[1] T. Ericson, *Phys. Rev. Lett.* **5**, 430 (1960).
[2] P. Brumer, M. Shapiro, *Adv. Chem. Phys.* **70**, 365 (1988).
[3] J.M. Petit, M. Henon, *Icarus* **66**, 536 (1986).
[4] B. Eckhardt, H. Aref, *Phil. Trans. R. Soc. A* **326**, 655 (1988).
[5] D.K. Campbell, M. Peyrard, P. Sodano, *Physica* **19D**, 165 (1986).
[6] B. Eckhardt, *Physica* **33D**, 89 (1988).
[7] U. Smilansky, Les Houches Session LII, Course X, ed. M.J. Giannoni, A. Voros, J. Zinn-Justin, Elsevier, Amsterdam, 1991.
[8] C. Jung, H.J. Scholz, *J. Phys. A* **20**, 3607 (1987).
[9] C. Jung, S. Pott, *J. Phys. A* **22**, 2925 (1989).
[10] C. Jung, *J. Phys. A* **23**, 1217 (1990).
[11] C. Jung, P.H. Richter, *J. Phys. A* **23**, 2847 (1990).
[12] C. Jung, S. Pott, *J. Phys. A* **23**, 3729 (1990).
[13] C. Jung, T. Tel, *J. Phys. A* **24**, 2793 (1991).
[14] T. Tel, *Directions in Chaos*, Vol.4 ed. B. Hao, World Scientific, Singapore, 1990.
[15] T. Tel, *J. Phys. A* **22**, L691 (1989).
[16] Z. Kovacs, T. Tel, *Phys. Rev. Lett.* **64**, 1617 (1990).
[17] V. Maslov, M. Fedoriuk, *Semiclassical Approximation in Quantum Mechanics*, Reidel, Dordrecht, 1981.
[18] J. Delos, *Adv. Chem. Phys.* **65**, 161 (1986).
[19] S. Knudson, J. Delos, B. Bloom, *J. Chem. Phys.* **83**, 5703 (1985).
[20] W.H. Miller, *Adv. Chem. Phys.* **30**, 77 (1975).
[21] P. Cvitanovic, B. Eckhardt, *Phys. Rev. Lett.* **63**, 823 (1989).
[22] M.V. Berry, *J. Phys. A* **10**, 2083 (1977).
[23] R. Blümel, U. Smilansky, *Phys. Rev. Lett.* **60**, 477 (1988).
[24] R. Blümel, U. Smilansky, *Phys. Rev. Lett.* **64**, 241 (1990).
[25] M.V. Berry, N.L. Balazs, *J. Phys. A* **12**, 625 (1979).
[26] M.C. Gutzwiller, *Chaos in Classical and Quantum Mechanics*, Springer, New York, 1990.
[27] P. Gaspard, S. Rice, *J. Chem. Phys.* **90**, 2242 (1989).
[28] M.L. Roukes, O.L. Alerhand, *Phys. Rev. Lett.* **65**, 1651 (1990).
[29] R.A. Jalabert, H.U. Baranger, A.D. Stone, *Phys. Rev. Lett.* **65**, 2442 (1990).
[30] C. Jung, in *The Electron*, ed. D. Hestenes, A. Weingartshofer, Kluwer, Dordrecht, 1991.
[31] R. Blümel, U. Smilansky, *Physica* **D36**, 111 (1989).
[32] G. Troll, U. Smilansky, *Physica* **D35**, 34 (1989).
[33] E. Doron, U. Smilansky, A. Frenkel, *Phys. Rev. Lett.* **65**, 3072 (1990).
[34] E. Doron, U. Smilansky, A. Frenkel, *Physica* **D50**, 367 (1991).

[35] P. Gaspard, S. Rice, *J. Chem. Phys.* **90**, 2255 (1989).
[36] W. John, B. Milek, H. Schanz, P. Šeba, *Phys. Rev. Lett.* **67**, 1949 (1991).
[37] M. Gutzwiller, *Physica* **D7**, 341 (1983).
[38] R. Blümel, B. Dietz, C. Jung, U. Smilansky, On the Transition to Chaotic Scattering, preprint.
[39] C. Jung, *J. Phys. A* **19**, 1345 (1986).
[40] C. Jung, *J. Phys. A* **20**, 1719 (1987).
[41] C. Jung, *J. Phys. A* **24**, 1741 (1991).